Modelling surface temperature and radiation budget of snow-covered complex terrain

Alvaro Robledano[1,2], Ghislain Picard[1], Laurent Arnaud[1], Fanny Larue[1], and Inès Ollivier[1]

[1]Univ. Grenoble Alpes, CNRS, IRD, Grenoble INP, IGE, 38000 Grenoble, France
[2]Univ. Grenoble Alpes, Université de Toulouse, Météo-France, CNRS, CNRM, Centre d'Etudes de la Neige, 38000 Grenoble, France

Correspondence: Alvaro Robledano (alvaro.robledano-perez@univ-grenoble-alpes.fr)

Abstract. The surface temperature controls the temporal evolution of the snowpack, playing a key role in ~~many physical processes such as metamorphism , snowmelt, ete~~metamorphism and snowmelt. It shows large spatial variations in mountainous areas because the surface energy budget is affected by ~~specific radiative processes that occur due to~~ the topography, ~~such as~~ for instance because of the modulation of the short-wave irradiance by the local slope, the shadows and the short-wave and long-wave re-illumination of the surface from surrounding slopes. These topographic effects are often neglected in large scale models considering the surface as flat and smooth. Here we aim at estimating the surface temperature ~~and the energy budget~~ of snow-covered ~~complex terrains~~mountainous terrain in clear-sky conditions, in order to evaluate the relative importance of the different processes that control the spatial variations. For this, a modelling chain is implemented to ~~derive~~ compute the surface temperature in a kilometre-wide area from local radiometric and meteorological measurements at a single station. The ~~main component~~ first component of this chain is the Rough Surface Ray-Tracing model (RSRT)~~, based~~ . Based on a photon transport Monte Carlo algorithm~~to quantify~~ , this model quantifies the incident and reflected short-wave radiation on every facet of ~~a mesh ,~~ the mesh describing the snow-covered ~~surface. RSRT is coupled to~~ terrain. The second component is a surface scheme ~~in order to estimate the complete~~ that estimates the terms of the surface energy budget from which the surface temperature is ~~solved~~eventually estimated. To assess the modelling chain performance, we use in situ measurements of surface temperature and satellite thermal observations (~~TIRS sensor aboard~~ Landsat-8) in the Col du Lautaret area, in the French Alps. The ~~satellite images are corrected from atmospheric effects with a single-channel algorithm. The~~ results of the simulations show (i) an agreement between the simulated and ~~observed~~ measured surface temperature at the station for a diurnal cycle in winter within ~~0.3~~0.2 °C; (ii) the spatial variations of surface temperature are on the order of 5 to 10 °C ~~between opposed slope orientations~~ in the domain and are well represented by the model; (iii) the ~~importance of the considered topographic effects is up to 1 , the most important being the~~ topographic effects ranked by importance are: the modulation of solar irradiance by the ~~topography~~local slope, followed by the altitudinal variations in air temperature ~~,~~ (lapse rate), the re-illumination by long-wave thermal emission from surrounding terrain ~~,~~ and the spectral dependence of snow albedo~~, and~~ . The changes in the downward long-wave flux because of variations in altitude and the absorption enhancement due to multiple bounces of photons in steep terrain play a less significant role. These results show the necessity of considering the topography to correctly assess the energy budget and the surface temperature of snow-covered complex terrain.

1 Introduction

~~The snow surface~~ The snow cover is rarely flat and smooth on Earth. Undulations exist over a very large range of scales, from the centimetre to the kilometre scale. At the centimetre and metre scales, ripples, snow dunes, and erosion features (sastrugi) formed by wind usually coexist (Filhol and Sturm, 2015). Penitents (spike formations of snow and ice – Lliboutry (1954)) are also found in some particular conditions. At the decametre to kilometre scale range, the snow surface topography is mostly determined by the underlying soil or ice topography (Revuelto et al., 2018). Because of all these undulations, the surface temperature can vary by several Celsius degrees across a study area, even without significant differences in the near-surface meteorological forcing (incident radiation, wind, air temperature, humidity). Terrain ~~tilt and~~ slope and orientation and the presence of facing neighbouring ~~terrains~~ slopes cause significant variations in the surface energy budget, and more specifically in the radiative components~~which comprise the short-wave (SW) and long-wave (LW) radiative fluxes~~. An abundant literature has investigated how ~~SW and LW~~ the short-wave (SW) and long-wave (LW) radiation is distributed across a complex terrain (Marks and Dozier, 1979; Duguay, 1993; Plüss and Ohmura, 1997), often for applications in mountainous areas. ~~Nevertheless, even if the literature for the smaller scales – that of the ripples, dunes, sastrugi and penitents – is usually distinct and scarcer, the principles equally apply to all the scales because the radiative transfers between faces are invariant by scale change. The exception is over long distances when the atmospheric scattering and absorption effects due to the air present between the terrain faces become significant (Lamare et al., 2020).~~

~~This study investigates and quantifies~~

This study aims at quantifying the relative importance of a series of topographic effects that control the ~~radiative~~ surface energy budget and the surface temperature. These effects are illustrated in Fig. 1 and summarized in Table 1. The first effect ~~,~~ ~~applying during daytime and under clear sky conditions, is the~~ is the combination of the shadowing from local horizons (cast shadows) and the modulation of the ~~solar irradiance received by a face depending on its~~ direct solar irradiance depending on the face slope and aspect relative to the sun's position. This modulation depends on the ~~cosine of the~~ local solar zenith angle (SZA). Self-shadowing occurs when the face completely turns away from the sun ~~, that is when the local solar zenith angle is below~~ (local SZA $<$ 0° or ~~over~~ $>$ 90°). Chen et al. (2013) accounted for this first effect, all the other terms of the energy budget being calculated as for flat terrain. This approximation is called "small slope approximation" by Picard et al. (2020) ~~which estimate it to be~~ and is valid for gentle slopes up to $\approx$ 20°.

Arnold et al. (2006) investigated the topographic parameters ~~that control~~ controlling the surface energy balance on an Arctic glacier. Their model takes into account not only the local ~~zenith angle~~ SZA and cast shadows for direct SW radiation, but also the sky view factor for the diffuse SW and sky LW radiation. The model additionally accounts for LW radiation from the surrounding slopes by assuming an average surface temperature, a simplification with respect to the reality where each face may have a different temperature. The model evaluated with measured melt rate in different parts of the glacier performs well (correlation coefficient r $\approx$ 0.85 for the majority of the melt season). The topographic effects ~~are ranked by order of importance in determining the surface energy budget, first shadowing, second the local zenith angle and third~~ ranked by importance are: first shadows, followed by the local SZA and the sky view factor. Olson et al. (2019) confirmed ~~these findings regarding the~~

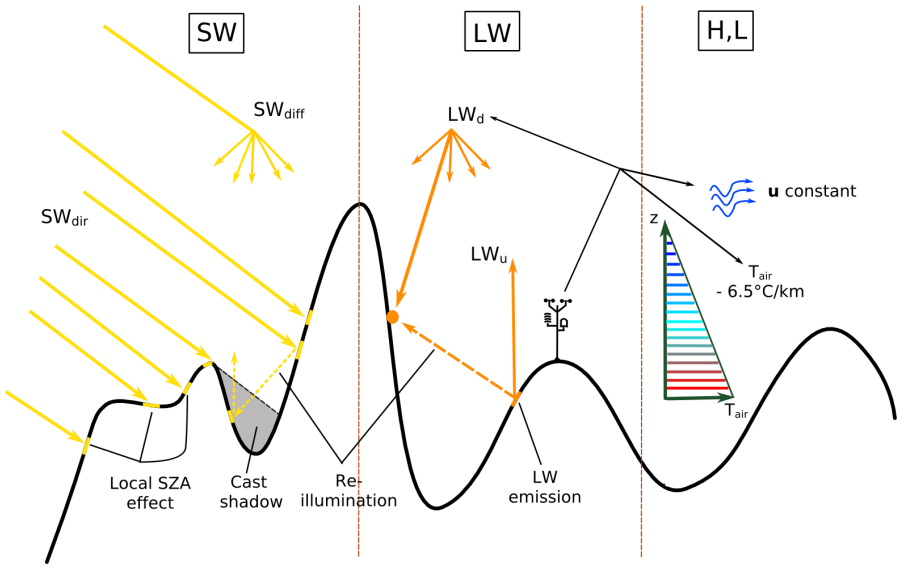

Figure 1. Illustration of the topographic effects considered in this study. They are summarized in Table 1.

two first effects. Arnold et al. (2006) also pointed out the role of the anisotropic reflectance of snow and ice, i. e. the fact that albedo is higher at higher solar zenith angles (Warren and Wiscombe, 1980). this ranking by studying the first two effects. LW emission by surrounding slopes can be a significant term in a steep topography. At larger scales (kilometre), Yan et al. (2016) showed that neglecting these topographic effects may induce errors of up to 100 Wm^{-2} for the modelled net LW flux.

Absorption enhancement due to multiple scattering within the topography is an additional effect, particularly important in steep terrains. It is indeed likely that the incident photons in such a terrain encounter more than one bounce between the terrain faces slopes before escaping to the sky or being absorbed in the snow. The total probability of absorption of a given incident photon is thereby increased by the successive at every bounce compared to over a flat or smooth surface where only at most one bounce occurs (Warren et al., 1998). Larue et al. (2020) experimentally quantified this effect by measuring spectral albedo over artificial rough surfacesand nearby smooth surfaces, effectively , showing a decrease of albedo (i.e. increase of absorption) of on the order of 0.03 – 0.08 in the visible and near-infrared compared to a smooth surface. This range was confirmed using optical SW-only in the SW using optical models for rough surfaces (Warren et al., 1998; Leroux and Fily, 1998; Lhermitte et al., 2014). For real 3D terrains, ray tracing ray-tracing and Monte Carlo techniques can take into account this effect (Larue et al., 2020), at the expense of intensive computation. Lee et al. (2013) used similar methods to show the impact of including the topography on the surface radiation budget over the whole Tibetan Plateau. They found differences of $\approx$14 Wm^{-2} with respect to a flat surface calculation. A simpler approach to account for multiple bounces is to add a mean contribution coming from neighbouring slopes, by assuming that the neighbouring faces they are illuminated as if they were flat (Lenot et al., 2009;

Olson et al., 2019). ~~More importantly, the~~ This contribution requires a value representing the effective albedo of neighbouring terrain and is modulated by the sky view factor of the slope. It is important to note that the absorption enhancement is not uniform~~on the surface. It~~ , it is usually stronger in the valleys (trapping effect~~or focusing) resulting in a higher ablation (melt or sublimation) observed in the valleys compared to that~~) than near the summits of the topography (Lliboutry, 1954). ~~When the scale of the surface roughness is of~~

In addition, most models cited above consider only broadband SW fluxes, neglecting the spectral dependence of snow albedo and incident radiation. The probable consequence is an inaccurate estimation of the absorption enhancement due to neglecting the large difference of albedo between the visible and the ~~order of~~ near-infrared. In the visible, the ~~ablation rate (e.g. crevasses, sastrugi, penitents, ...), this differential ablation can significantly affect the topography, and in fact can increase the amplitude of the terrain undulations, and thus further increase absorption. This positive feedback loop is key to explain the formation of penitents (Cathles et al., 2014) (and refs therein)and suncups (Betterton, 2001). The energy balance model developed by Cathles et al. (2011) and Cathles et al. (2014) to explore this feedback considers 2D roughness (e.g. a linear crevasse) and computes absorptionin every small element of the surface. While their model includes shadowing, local zenith angle and multiple bounces, it neglects the view factor on sky LW radiation and emission by the faces, which could further enhance absorption in the valleys. Corripio and Purves (2005) also investigated penitent formation, and accounts for LW radiation and sky view factor effect with a similar approach to that of Arnold et al. (2006) for mountains. LW emission by faces can be a significant term in a steep topography, as in penitents. At larger scales (kilometre), Yan et al. (2016) showed that neglecting topography effects may induce errors of up to 100 for the modelled LW net flux. Lee et al. (2013) used 3-D Monte Carlo photon tracking methods to show the impact on surface radiation budget over the Tibetan Plateau, finding deviations in surface solar fluxes on the order of 14~~ albedo is high (typically over 0.95), implying intense multiple scattering but extremely weak absorption. In contrast, the albedo is lower in the near-infrared and closer to the optimal albedo for enhancement (0.5), where multiple scattering and absorption are balanced (Warren et al., 1998).

The turbulent heat fluxes are ~~of significant importance~~ important in the surface energy budget ~~, as shown by Brun et al. (1989) . They are capital in snow-covered areas, and in~~ (Brun et al., 1989), in particular during nights, as they balance the radiative cooling of the surface. These fluxes are difficult to parameterized ~~as~~ when only a few in situ measurements are ~~usually available , and only at a single level~~ available (Martin and Lejeune, 1998; Pomeroy et al., 2016). In complex terrain, their spatial and temporal variations are mostly determined by the wind distribution around the relief and by the change of air temperature with elevation (Rotach and Zardi, 2007).

The most advanced model to simulate surface temperature in a mountainous area is – to our knowledge – a commercial product (Adams et al., 2009, 2011) which includes not only a comprehensive energy budget modelling (inc. absorption enhancement and emission by faces), but also radiation penetration in the snow, different types of surface (snow, rock, tree) and the heat diffusion in the snow to describe the full temperature profile in the snowpack~~for each face~~. The precise equations and approximations are however not known. In a study case in southwest Montana, USA, the model predicts spatial variations of temperature between -15 °C and 0 °C at 2 pm local time, with most of these variations being primarily explained by terrain type. This non-exhaustive review of approximations and models in the literature highlights the various effects related to

the topography, the large number of possible approximations and the ~~degrees of complexity used at both~~ different scales of application (metre-scale roughness and complex-terrain scales~~. These effects and approximations are summarized in Table 1 and illustrated in Fig. 1.~~).

~~Illustration of the several topographic effects that are considered in this study. Common approximations for the calculation of these effects are summarized in Table 1.~~

~~In addition, most models cited above consider only broadband SW fluxes, neglecting the spectral dependence of snow albedo and incident radiation. The probable consequence is an inaccurate estimation of the absorption enhancement due to neglecting the large difference of albedo between visible and near-infrared. In the former domain, the albedo is high (typically over 0.95), implying intense multiple scattering but extremely weak absorption. In contrast, in the near-infrared the albedo is lower and closer to the optimal albedo for enhancement (0.5), where multiple scattering and absorption are balanced (Warren et al., 1998)~~ .

Table 1. Several effects relevant to short-wave (SW), long-wave (LW) and turbulent heat fluxes calculation in complex terrains~~and rough surfaces~~. Other effects such as those involving the atmosphere are beyond the scope of this study.

~~Effect~~ Topographic effect	~~Spectral domain and illumination~~ Energy flux
~~Variations of illumination angles and self~~ Cast shadows	Direct SW
~~Cast shadows~~Variations of the local solar zenith angle (self shadows)	Direct SW
~~Anisotropy of reflectance~~ Face re-illumination / absorption enhancement	SW
Spectral variations in albedo and irradiance	SW
~~Face re-illumination / absorption enhancement SW~~ Reduced sky view	Diffuse SW and LW
~~Face thermal emission~~ Thermal emission from surrounding terrain	LW
Altitudinal changes in air temperature	Turbulent heat fluxes (H, L)

To investigate the relative importance of the topographic effects, this study aims at ~~estimating~~ modelling the snow surface temperature variations in a mountainous area ~~with a modelling chain that uses local in situ~~ from radiometric and meteorological measurements ~~from a single station. The~~ at a single point. The modelling chain includes a 3D radiative transfer model, the Rough Surface ~~Ray Tracer~~ Ray-Tracing (RSRT) model (Larue et al., 2020), ~~which~~ to compute the incident and reflected SW radiation. The model launches a set of photons to the snow surface described by a triangular mesh ~~,~~ (i.e. a connected set of triangular facets), that can be derived easily from a Digital Elevation Model (DEM). Its spatial resolution limits the scope of this study to topography at the decametre to kilometre scale range. The RSRT simulation results are then used in a surface scheme (RoughSEB model) to compute the ~~short-wave and long-wave net~~ net SW and LW radiation and the turbulent heat fluxes on each facet ~~. Eventually the surface temperature is deduced. Satellite~~ as a function of the facet surface temperature.

The surface temperature is eventually deduced by closure of the energy budget. To assess the modelling chain performance, satellite thermal infrared observations from Landsat-8 are used~~in order to evaluate the modelled spatial variations. To quantify the relative importance of the topographic effects, additional simulations are run disabling one single effect at a time and~~. The topographic effects that are taken into account in this study can be disabled or modified when needed, in order to quantify their relative importance by measuring the impact on the surface temperature. This study is applied at the Col du Lautaret area ~~, in the French Alps~~(French Alps), and we mostly consider clear-sky conditions since they tend to maximize the topographic effects compared to diffuse conditions. Sect. 2 provides the model description, as well as the method for retrieving surface temperature from satellite images and a description of the study area. Results are shown in Sect. 3, and discussed in Sect. 4. ~~Final remarks and conclusion are addressed~~ Conclusion is presented in Sect. 5.

2 Methods and materials

2.1 The RoughSEB model

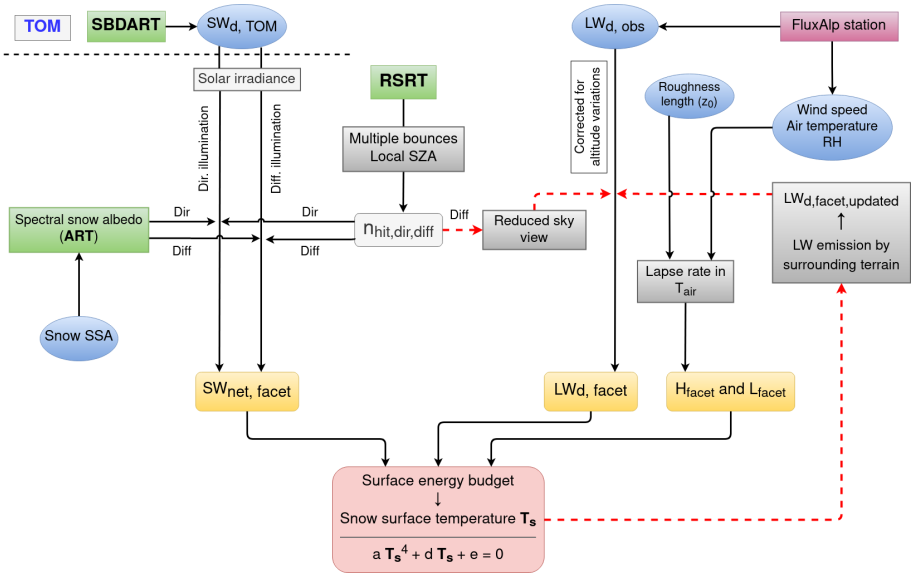

Figure 2. Flowchart of the modelling chain to estimate snow surface temperature. TOM (top of mountains) is the horizontal above the highest point in the study area. The ~~models~~ involved models are in green, ~~and~~ the terms of the surface energy budget are in orange, the needed inputs are in blue and the topographic effects are in grey. The red dashed lines indicate the ~~last steps of~~ two-step iterative process to compute the ~~chain~~downward LW flux.

Snow surface temperature (T_{ss}) is obtained by solving the surface energy budget equation ~~. Each term of this equation is estimated with a chain of existing and new models depicted in Fig. 2.~~ for each facet of the modelled snow surface. The energy budget comprises (Arya, 1988): (i) the net radiation fluxes, which are split into the contributions of the short-wave radiation

from 0.3 µm to ~~24~~ 4 µm (SW_{net}) and the long-wave radiation from ~~23~~ µm to 100 µm (LW_{net}); (ii) the sensible heat flux (H), which ~~measures~~ arises as a result from the exchange of heat between the surface and the air just above; (iii) the latent heat flux (L) resulting from water state changes (sublimation or condensation) at the surface and exchange with the air above, and (iv) the ground heat flux (G), which is transferred to the snowpack and lead to a change of snow temperature or melt. Here, we ~~consider only temperature estimation and~~ assume below freezing temperature so that melt is not involved. The sum of these fluxes is null according to the first principle of the thermodynamics, ~~taking into account that~~ since the surface has no internal enthalpy:

$$SW_{net} + LW_{net}(T_s) + H(T_s) + L(T_s) + G = 0 \quad (1)$$

~~In the RoughSEB model, all these~~ Each term of this equation is estimated with a chain of existing and new models depicted in Fig. 2. All the constant terms are calculated for each facet (hereafter noted with the subscript f)~~of the modelled snow surface .~~, and the rest are calculated as a function of the facet temperature. The snow surface temperature is eventually estimated for each facet of the modelled surface, by closure of the energy budget (Sect. 2.1.4).

The computation of the SW_{net} radiation (Sect. 2.1.1) involves: (i) the Santa Barbara DISORT Atmospheric Radiative Transfer model (SBDART – Ricchiazzi et al. (1998)), an atmospheric model that simulates the incoming spectral irradiance above the studied area (top of mountains – TOM), and (ii) the RSRT model (Larue et al., 2020), based on a Monte Carlo photon tracking algorithm that computes the path of the photons launched towards the surface and allows considering the modulation of SW radiation by the terrain slope and aspect. The simulations are ~~run in both~~ done separately for the direct and diffuse ~~illumination conditions~~ components of the short-wave irradiance (noted with subscripts dir and diff)~~, and~~ . Moreover, the atmospheric effects (i.e. atmospheric attenuation, clouds) are neglected within the studied ~~area~~ domain (between the surface and TOM). The scene is ~~also~~ considered to be covered by ~~pristine,~~ pure snow (i.e. no impurities), which ~~is applicable~~ applies in winter. The calculation of the LW_{net} radiation (Sect. 2.1.2) needs the downwelling LW flux, measured by a local station ~~representative of the area, and~~ and corrected for altitude variations within the domain. It is subsequently updated by accounting for the reduced sky-view factor of each facet and the thermal emission of surrounding terrain~~as in Arnold et al. (2006). The effect of the~~ . The turbulent heat fluxes (H and L) ~~, while being considered, is not the main objective of this work. They~~ are computed with a simplified approach (Sect. 2.1.3) that involves common in situ meteorological measurements (i.e. air temperature, wind speed and relative humidity) and introduces a lapse rate effect.

~~The snow surface temperature (Sect. 2.1.4) is eventually estimated for each facet of the modelled surface. The topographic effects that are taken into accountin this study can be disabled or modified when needed, allowing to quantify their relative importance.~~

2.1.1 Calculation of the short-wave radiation fluxes

~~In order to consider~~

The calculation of the SW_{net} radiation takes into account: (i) the topographic effects affecting the SW radiation~~and~~ , and (ii) the spectral dependence of snow albedo and incident ~~radiation, the calculation of the net SW radiation needs to be carefully~~

~~performed~~solar irradiance. The aim is to compute it on every facet f due to the direct and diffuse ~~irradiation~~components of the solar irradiance:

$$SW_{\text{net, f}}(\theta_s) = SW_{\text{net, dir, f}}(\theta_s) + SW_{\text{net, diff, f}} \tag{2}$$

$$SW_{\text{net, dir, f}}(\theta_s) = \int_{\lambda_0}^{\lambda_1} \mathrm{A}_{\text{dir, f}}(\lambda, \theta_s)\, \mathrm{I}_{\text{dir}}(\lambda)\, d\lambda \tag{3}$$

$$SW_{\text{net, diff, f}} = \int_{\lambda_0}^{\lambda_1} \mathrm{A}_{\text{diff, f}}(\lambda)\, \mathrm{I}_{\text{diff}}(\lambda)\, d\lambda \tag{4}$$

where the direct and diffuse components of the absorbed SW radiation by every facet are computed using: (i) an absorption coefficient $\mathrm{A}_{\text{dir, diff, f}}$, derived from the RSRT model, and (ii) the spectral irradiance coming from the sky ~~(~~$\mathrm{I}_{\text{dir, diff}}(\lambda)$~~)~~, issued from the SBDART model. The integration ~~limits (~~is between λ_0 ~~and λ_1) are respectively equal to~~ = $300\,\mathrm{nm}$ and ~~2000~~λ_1 = $4200\,\mathrm{nm}$, to cover all the solar radiation spectrum.

A ~~naive~~ direct way to compute ~~these terms~~ the absorbed SW radiation by each facet would be to use the ray-tracing RSRT model to trace many photons for every wavelength in the solar spectrum~~to compute the absorbed SW radiation by each facet~~. Nevertheless, with millions of facets and hundreds of wavelengths, this approach would imply an enormous computational cost, due to the inefficiency of the Monte Carlo ~~ray tracing~~ ray-tracing method. To overcome this, ~~an alternative approach consists of taking~~ we take advantage of the result of the RSRT model to account for multiple bouncing~~provided a few assumptions. The RSRT model can indeed compute~~. In this model, each launched photon has an initial propagation direction specified by the zenith and azimuth angles and a random initial position above the mesh. The intersection between the photon direction and the mesh surface is first calculated. Then, to simulate a Lambertian reflection, the change of direction is taken randomly from the cosine-weighted hemispherical distribution. The algorithm iterates as long as the photon propagates from facet to facet, and stops only when the photon escapes from the domain or when a maximum number of bounces is reached (noted n_{max}). No albedo and no absorption are involved at this stage, RSRT only computes possible geometric trajectories of photons in the given mesh. The number of photons launched is $4{\cdot}10^8$, and edge effects are avoided by excluding the outermost 15% of the mesh area.

The RSRT model records the number of times ~~a photon has~~ photons have hit a given facet ~~regardless of the albedo (and so of the wavelength), according to the~~ as a function of the bounce order of the photon (first reflection, second reflection, ...). Noted $\mathrm{n}^{(i)}_{\text{hit, d, f}}$, it corresponds to the proportion of photons that directly hit the facet ~~on~~ at their i^{th} ~~hit (d being~~ reflection (from i = 0, and d is dir or diff depending on the illumination conditions – direct or diffuse).

~~Assuming~~ Assuming that the area has an uniform albedo (same snow properties ~~) and the reflection is~~ everywhere in the domain) and that the reflections are Lambertian, the absorption coefficient $\mathrm{A}_{\text{dir, diff, f}}$ is computed by taking into account: (i) the spectral dependence of snow albedo, and (ii) the fact that the illumination received by each facet ~~depends on the cosine of the local solar zenith angle and the absorption enhancement produced by multiple bouncing,~~ is the sum of the illumination from

photons at their first reflection and the multiple bounce contribution, considered as diffuse illumination from photons at their second reflection, third reflection, etc. The coefficient is determined with:

$$A_{\text{dir, f}}(\lambda,\theta_s) = [1-\alpha_{\text{dir}}(\lambda,\theta_s)]\, n^{(0)}_{\text{hit, dir, f}} + \left[1-\alpha_{\text{diff}}(\lambda)\right] \alpha_{\text{dir}}(\lambda,\theta_s) \sum_{i=1}^{i=n_{\max}} \alpha^{i-1}_{\text{diff}}(\lambda)\, n^{(i)}_{\text{hit, dir, f}} \quad (5)$$

$$A_{\text{diff, f}}(\lambda) = [1-\alpha_{\text{diff}}(\lambda)] \sum_{i=0}^{i=n_{\max}} \alpha^{i}_{\text{diff}}(\lambda)\, n^{(i)}_{\text{hit, diff, f}} \quad (6)$$

where θ_s is the local solar zenith angle and $\alpha_{\text{dir, diff}}(\lambda,\theta_s)$ is the snow spectral albedo ~~in both~~ under direct and diffuse illumination. Here, ~~it is~~ these albedos are computed using the Asymptotic Radiative Transfer (ART) theory (Kokhanovsky and Zege, 2004)~~. Its expression~~ , whose formulation is presented in the Appendix A1~~, provided several assumptions about the snowpack (semi-infinite, vertical and horizontal homogeneous layers) and the surface (flat and smooth – facets are small enough to be considered as it). It considers~~ . The calculation needs the snow specific surface area (SSA) ~~, which is needed as input~~as input. If not specified, a standard value of 20 $\mathrm{m^2 kg^{-1}}$ is assumed in the modelling~~chain.~~ .

The spectral irradiance coming from the sky $I_{\text{dir, diff}}(\lambda)$ is computed with the SBDART model. This model computes the atmospheric transmission and scattering (Mie theory). The simulations are run in the spectral range 300 – 4200 nm, by steps of 3 nm. Here, a generic mid-latitude winter atmospheric profile is assumed and the aerosol optical depth at 550 nm is 0.08 ("rural" profile in SBDART). The elevation is 2052 m.a.s.l. (see Sect. 2.2) and solar zenith and azimuth angles correspond to the desired date and time.

The net broadband SW radiation ~~per facet is therefore~~ of each facet is eventually calculated by means of ~~Eqs~~Eq. (2~~, 5, 6), previously accounting for the spectral irradiance coming from the sky and integrating each component over the 300 - 2000 wavelength range~~).

2.1.2 Long-wave radiation fluxes

~~The downwelling LW flux at the top of the mountains~~ To compute the incident LW flux from the atmosphere on each facet, we first apply a local correction to the observed downward LW flux (noted $\text{LW}_{\text{d, TOM}}$)~~is issued from in situ measurements~~ ($_{\text{d, obs}}$), measured in a single point of the domain (Sect. 2.2)~~and considered constant across the scene regardless of the variations of altitude. To compute the~~ . This correction takes into account the LW variations in altitude over the whole domain, using the same approach as in Arnold et al. (2006). The correction consists in deriving an "effective emissive temperature" of the sky (noted $T_{\text{sky, obs}}$) from the measured LW flux with the Stefan-Boltzmann equation. This temperature is corrected for changes in elevation by introducing the lapse rate Γ:

$$LW_{\text{d, obs}} = \sigma\, T^4_{\text{sky, obs}} \quad (7)$$

$$T_{\text{sky, f}} = T_{\text{sky, obs}} + \Gamma\,(z_f - z_{\text{obs}}) \quad (8)$$

with σ the Stefan-Boltzmann constant and where $T_{\text{sky, f}}$ is the effective emissive temperature of the atmosphere above each facet. We choose Γ = -6.5 °C km^{-1}, the environmental lapse rate as defined in the International Standard Atmosphere (ISO 2533:1975). The downwelling LW flux incident on each facet ~~, we proceed~~ ($LW_{\text{d, f}}$) is then recalculated with the Stefan-Boltzmann equation:

$$LW_{\text{d, f}} = \sigma \, T_{\text{sky, f}}^4 \tag{9}$$

In complex terrain facets not only receive radiation from the atmosphere but also from the surrounding slopes. Computing this contribution requires the facet surface temperature, which is precisely unknown. We proceed by iteration in two steps~~. In~~ : in the first step, we ~~consider the surface as flat so that all the facets receive the TOM LW radiation and no~~ neglect the thermal emission from the surrounding ~~slopes~~facets. This leads to a first estimate of the surface temperature (Sect. 2.1.4), that is then used in the second step to account for the emission of surrounding ~~slopes by computing the average upwelling long-wave~~ terrain. The average upwelling LW flux from each facet ~~as in Arnold et al. (2006), and using~~($LW_{\text{u, scene-average}}$) is computed from the average surface temperature of the whole domain with the Stefan-Boltzmann equation. This thermal emission is a constant, we neglect the possible variations of temperature around each facet. The updated downwelling LW flux on each facet is eventually calculated with:

$$LW_{\text{d, f, updated}} = V_{\text{f}} \, LW_{\text{d, TOM}\,\text{d, f}} + (1 - V_{\text{f}}) \, LW_{\text{u, scene-average}} \tag{10}$$

where V_{f} is the sky-view factor ~~estimated~~ calculated with RSRT. V_{f} is different for each facet~~so that facets~~ : those in the valley receive more ~~energy~~ LW radiation from the surrounding slopes than facets at the summits of the ~~mountains. It~~ domain. The sky-view factor is indeed equal to the proportion of the launched photons hitting a facet on their first bounce in diffuse illumination, namely $\text{V}_{\text{f}} = n^{(0)}_{\text{hit, diff, f}}$. ~~However, $LW_{\text{u, scene-average}}$ is a constant, we neglect the possible variations of temperature around each facet.~~

~~For the~~ The upwelling long-wave radiation, $LW_{\text{u, f}}$ is determined by the Stefan-Boltzmann law:

$$LW_{\text{u, f}} = \epsilon \, \sigma \, T_{\text{s}}^4 + (1 - \epsilon) \, LW_{\text{d, f}} \tag{11}$$

with snow emissivity $\epsilon = 0.98$ ~~, σ the Stephan-Boltzmann constant~~ and T_{s} the snow surface temperature of the facet.

2.1.3 Turbulent heat fluxes

While the main focus of this work is on the role of the topographic effects controlling the ~~radiative~~ radiation budget of the surface, the turbulent heat fluxes ~~needs~~ need also to be assessed to ~~compute the~~ close the surface energy budget. We follow a ~~very~~ simple modelling approach~~at this stage~~, potential improvements are let to further work in the future. The sensible and latent heat fluxes are calculated following the one-level approach:

$$H_{\text{f}} = \rho_{\text{air}} \, c_{\text{p, air}} \, C_{\text{H}} \, U \, (T_{\text{s}} - T_{\text{air}}) \tag{12}$$

$$L_{\text{f}} = L_s \, \rho_{\text{air}} \, C_{\text{H}} \, U \cdot (q_{\text{sat}}(T_{\text{s}}, P_{\text{s}}) - q_{\text{air}}) \tag{13}$$

where ρ_{air} and $c_{p,air}$ are the density and heat capacity of the air, U is the wind speed, T_{air} is the air temperature, L_s is the sublimation heat, $q_{sat}(T_s, P_s)$ is the specific humidity at snow surface temperature T_s and pressure P_s, and C_H is a surface exchange coefficient. In principle this coefficient depends on atmospheric stability but for the sake of simplicity, a neutral situation is considered here. C_H therefore depends only on the aerodynamic roughness length z_0, assumed constant across the ~~scene~~ domain and equal to 10^{-3} m following previous works (Brock et al., 2006). The expression of this coefficient is provided in the Appendix A2, and the values of the ~~symbols defined here~~ defined symbols are presented in the Table B1. The air temperature and wind speed are ~~given from a meteorological station in the scene~~ taken from the meteorological station (Sect. 2.2). ~~To account for the differences~~ T_{air} accounts for the variations in altitude within the ~~scene, the lapse rate Γ is taken into account:~~

$$T_{air,\,f} = T_{air,\,obs} + \Gamma\,(z_f - z_{obs})$$

~~where $T_{air,\,f}$ is the air temperature over the facet f. We choose Γ = -6.5 , the environmental lapse rate as defined in the International Standard Atmosphere (ISO 2533:1975).~~ domain in a similar way as the downward LW flux (Sect. 2.1.2), via a lapse rate effect (Eq. 8). Wind speed and relative humidity are however considered constant. Note that the specific humidity ~~being~~ is deduced from the relative humidity and air temperature, so it indirectly depends on altitude.

The ground heat flux (G) is here neglected as the snowpack is considered thermalized~~, meaning~~ . We assume that no energy is exchanged with the snowpack~~. This assumption~~ , which is checked in the discussion (Sect. 4.2)~~with regard to our results~~.

2.1.4 Snow surface temperature estimation

The equation of the surface energy budget (Eq. 1) ~~is to be solved for~~ with explicit T_s dependencies is:

$$SW_{net,\,f} + LW_{d,\,f,\,updated} - LW_{u,\,f}\left(\mathbf{T_s}^4\right) + H_f\left(\mathbf{T_s}\right) + L_f\left(q_{sat}(\mathbf{T_s})\right) = 0 \tag{14}$$

The equation is solved to determine the unknown T_s for each facet f. However this equation is non-linear due to the ~~T_s^4~~ T_s^4 term (upwelling LW radiation) and the complex dependence of the surface specific humidity to ~~T_s~~ T_s. Solving such an equation for millions of facets can be computationally intensive. To avoid this issue, we linearize the specific humidity at saturation about T_{air}, as in Essery and Etchevers (2004):

$$q_{sat}(T_s, P_s) = q_{sat}(T_{air}, P_s) + (T_s - T_{air}) \cdot q'_{sat}(T_{air}, P_s) \tag{15}$$

where:

$$q'_{sat}(T_{air}, P_s) = \left(\frac{q_{sat}(T_{air}, P_s) - q_{sat}(T_{air} - \Delta T, P_s)}{\Delta T}\right) \tag{16}$$

~~with a~~ with ΔT = 5 K. The simplified surface energy budget equation eventually ~~become~~ becomes a quartic equation for T_s of the form:

$$a\,T_s^4 + d\,T_s + e = 0 \tag{17}$$

where a, d, e are a constant (for each facet). The general solution (Neumark, 1965) of this equation is shown in the Appendix A3~~for completeness~~. The evaluation of this equation for a large number of facets is computationally ~~very~~ efficient compared to using a non-linear optimization ~~technique~~solver.

2.2 ~~Description of the existing models~~

~~The modelling chain involves two existing models, namely the SBDART model (Ricchiazzi et al., 1998) and the RSRT model (Larue et al., 2020). Here we briefly describe the parameters to run them in the present work.~~

~~The SBDART model provides the short-wave irradiance spectrum at the top of the mountains. It considers several atmospheric transmission models and the Mie theory to take scattering into account. The simulations are run in the spectral range 300 – 2000 , by steps of 3 . In our case, a generic mid-latitude winter atmospheric profile is assumed and the aerosol optical depth at 550 is 0.08 ("rural" profile in SBDART). The elevation is 2052 m.a.s.l. (see Sect. 2.2) and solar zenith and azimuth angles corresponding to the desired date and time.~~

~~RSRT model provides the number of photon hits on each facet according to its bounce order, noted $n_{\text{hit, d, f}}^{(i)}$. In this model, each launched photon has an initial propagation direction $\boldsymbol{i}$, specified by the zenith and azimuth angles, and a random initial position over the mesh. Edge effects are avoided by excluding the outermost 15% of the mesh. The model calculates the propagation with the following main steps: (1) estimation of the next intersection between the photon path and the mesh; (2) determination of the reflection direction (random cosine-weighted hemispherical distribution in our case to simulate Lambertian reflection), and (3) update of the direction $\boldsymbol{i}$. The algorithm iterates until the photon escapes from the scene or up to a maximum number of bounces of 15. The number of facets in the mesh is typically 10^6 and the number of photons launched is $4{\cdot}10^8$.~~

2.2 Study area and in situ measurements

Figure 3 shows the study area. It is located around the ~~Col du Lautaret~~ Lautaret mountain pass in the French Alps (45.0°N, 6.4°E). This area is ~~interesting for studying~~ of interest to study surface temperature, as it features both north and south-facing slopes ~~, in addition to~~ that are spaced by a few hundreds of meters. It also contains smaller-scale rugged terrain covering the rest of orientations and promoting re-illumination. The size of the area is $\approx 50\,\mathrm{km}^2$ ~~, with a large diversity of rough features.~~and the range of altitudes spans from 1640 to 3220 m.a.s.l. The predominant orientation is S-SW, followed by N-NE facing terrain, and the slope varies mainly between 15° and 40°. Protruding vegetation is rare in the study area in winter and is neglected here. We assume that the snow cover is 100%. The mesh required for simulations was built from the RGE ALTI®Version 2.0 Digital Elevation Model (DEM) provided by IGN France (IGN, 2021), acquired using radar techniques in 2009. Its coordinate reference system is Lambert 93 (EPSG: 2154), and the original spatial resolution was of $5\,\mathrm{m}$. It was however resampled to $10\,\mathrm{m}$ ~~due to computational limitations~~to limit computational cost. To create the mesh, the centre of each pixel is ~~a vertex that is connected to its~~ taken as a vertex. Each vertex is then connected to their 4 closest neighbours, which eventually leads to two triangular facets shared by the same vertex.

The study area ~~also~~ includes the measurement station FluxAlp (45.0413°N, 6.4106°E), ~~on the Pré des Charmasses site.~~located at 2052 m.a.s.l. This station collects meteorological and radiometric observations~~, and its description can be found in Dumont et al. (2017)~~

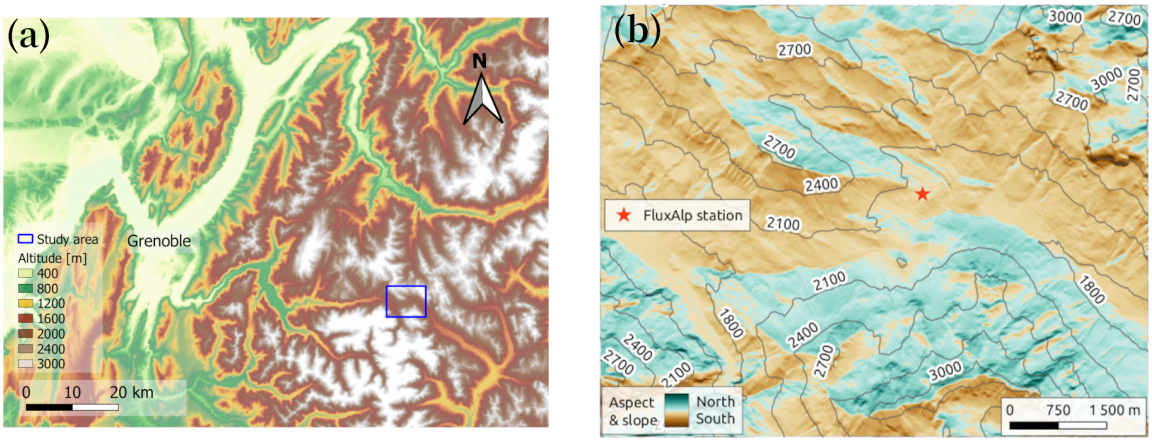

Figure 3. Location of the study area, around the Col du Lautaret alpine site. The blue rectangle in (a) represents the ~~hillshade image~~ extension of the study area, shown in (b). ~~It~~ The domain is generated from the RGE ALTI®Version 2.0 Digital Elevation Model (DEM) provided by IGN France ~~with~~ at a spatial resolution of 5 m, and resampled to 10 m for ~~computational limitations~~this study. ~~The windrose shows~~ Slope angle is represented by the ~~distribution~~ intensity of the ~~terrain slopes as a function of the aspect~~color.~~The radius of each of the 16 sectors corresponds to the normed (displayed in percent) quantity of facets.~~

. Radiation fluxes are measured with a Kipp & Zonen CNR4 radiometer with spectral range (0.3 - 2.8 µm in the SW, 4.5 - 42 µm in the LW). The data needed as input for the modelling chain is issued from here (~~meteorological –~~ air temperature, wind speed, relative humidity and ~~radiometric – downwelling long-wave~~ downwelling LW radiation flux). ~~The latter is assumed to be equal to that received above the area (TOM), as the LW re-illumination at the station is very low according to initial tests of the modelling chain. FluxAlp~~ All measurements are averaged over 30 min, i.e. a measurement at ~~10h30~~ 10:30 UTC is the average of the period ~~10h00~~ 10:00 UTC – ~~10h30~~ 10:30 UTC. The upwelling LW measurements at FluxAlp are used to assess the modelled surface temperature ~~temporal variations in a single point. They are complemented by a spatially distributed surface temperature dataset described in the following section.~~ at the station point.

~~In addition to the automatic measurements , manual measurements of~~ Manual measurements of surface snow SSA for two consecutive winter seasons (2016 / 2017 and 2017 / 2018) have been collected occasionally (Tuzet et al., 2020), a few meters around the FluxAlp station. The measurements were collected with the DUFISSS instrument (Gallet et al., 2009) during the first season, and with the Alpine Snowpack Specific Surface Area Profiler (ASSSAP, a lighter version of POSSSUM instrument (Arnaud et al., 2011) during the second season. These measurements have an estimated uncertainty of 10 %.

2.3 Surface temperature retrieval with Landsat-8 observations

Spatial variations of surface temperature are retrieved from satellite observations. The two thermal bands (TIRS – Bands 10 and 11) onboard Landsat-8 cover the spectrum ~~between~~ at around 10.6 µm ~~to~~ and 12.51 µm, with a spatial resolution of 100 m (resampled by ~~Cubic Convolution~~ cubic convolution methods to 30 m in the product) and a 16 day repeat cycle. Different methods to correct atmospheric effects have been implemented in order to retrieve Land Surface Temperature (LST, hereafter)~~, based on~~ : split-window methods (Jin et al., 2015), mono-window techniques (Tardy et al., 2016), or ~~a~~ single-channel ~~approach~~ approaches (Jiménez-Muñoz and Sobrino, 2003). Soon after the launch of Landsat-8, stray light was observed on thermal data (Montanaro et al., 2014), ~~coming from~~ due to scattering of outer radiance in Band 11. Methods based on only one band are therefore suggested~~, so here we apply a~~ . The single-channel approach ~~, which consists of approximating~~ proposed by Jiménez-Muñoz and Sobrino (2003) approximates the atmospheric functions from the atmospheric water vapour content (w, in g cm^{-2}). Cristóbal et al. (2018) presented an improved single-channel method dependent not only on water vapour content, but also on near-surface air temperature (T_a)~~, which are available from reanalysis data. The recently available Landsat Collection 2 Surface Temperature product is also considered here and compared to the results of the aforementioned LST retrieval methods in our particular case of study.~~ . Figure 4 shows the flowchart to retrieve LST from satellite observations, following Cristóbal et al. (2018).

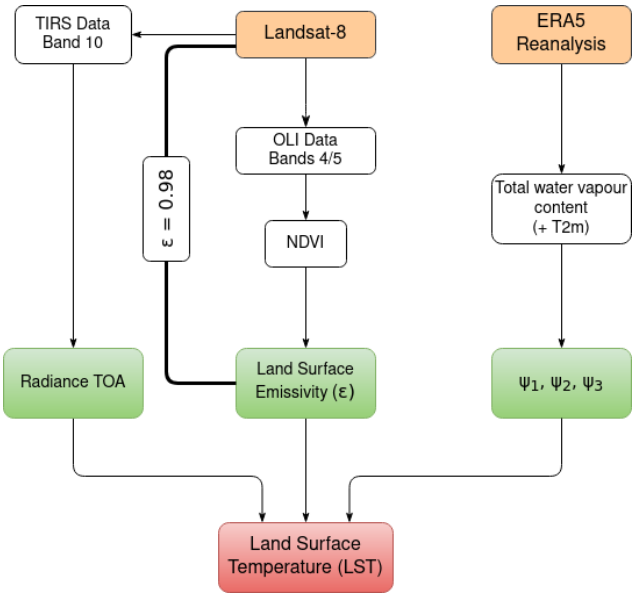

Figure 4. Workflow to retrieve Land Surface Temperature from Landsat-8 thermal observations with a single-channel approach.

Both the single-channel method (SC method – Jiménez-Muñoz and Sobrino (2003)) and the improved single-channel method (iSC method – Cristóbal et al. (2018)) have been implemented in this study. LST is calculated for each pixel by applying the

radiative transfer equation to a sensor channel (Eqs. (1) to (3) in Cristóbal et al. (2018)), which eventually leads to:

$$LST = \gamma \cdot \left[\varepsilon^{-1} \left(\psi_1 \cdot L_{\text{sensor},\lambda} + \psi_2\right) + \psi_3\right] + \delta \quad (18)$$

where γ and δ are constants that depend on the top of atmosphere radiance ($L_{\text{sensor},\lambda}$) and the brightness temperature of the pixel, ε is the emissivity of the pixel and ψ_i are the atmospheric ~~functions that are parameterized~~ parameterized functions. More details are shown in Appendix A4 for completeness. The emissivity is considered equal to 0.98 on the whole scene, in line with our modelling chain. Water vapor and near-surface air temperature data come from ERA5 Reanalysis dataset (Muñoz Sabater, 2019). They are taken from the closest grid point. In order to cover a large range of solar zenith angles, a total of 20 cloudless thermal images from different winter dates were selected, from February 2015 to December 2019 (list in ~~the appendix~~Appendix C). The acquisition time of Landsat-8 observations (~~10h17 or 10h23~~ 10:17 or 10:23 UTC depending on the scene) and in situ measurements (~~10h30~~ 10:30 UTC, averaged over the previous 30 min) are considered to be equivalent. Among the selected clear-sky days, four of them have accompanying manual measurements of snow SSA (Tuzet et al., 2020). These are 2 February 2018, 18 February 2018, 27 February 2018 and 22 March 2018, with snow SSA of 47, 45, 53 and 32 $\mathrm{m^2 kg^{-1}}$, respectively.

The Landsat Collection 2 Surface Temperature product made recently public is also considered here. It is compared to the results of the aforementioned LST retrieval methods in our case of study.

3 Results

The spatially-resolved LST observations from Landsat-8 are first assessed in the study area, before the evaluation of the model simulations against the ~~observations and the local measurements .~~ local measurements and the satellite observations. Finally the relative importance of the topographic effects on surface temperature is quantified.

3.1 Surface temperature observations from Landsat-8

The surface temperature observations from Landsat-8 (LST) are compared to the in situ FluxAlp measurements (Fig. 5a). The ~~surface temperature from Landsat-8~~ Landsat-8 surface temperature is extracted from the pixel covering ~~the location of FluxAlp from all~~ FluxAlp station location from all the 20 thermal images. Both the single-channel (SC) method and the improved single-channel (iSC) method show better estimations at FluxAlp station than the official Collection 2 Surface Temperature product (-3.5 °C underestimation). As a result, we ~~excluded~~ exclude this latter dataset from further analysis. The iSC method provides generally higher temperatures than the SC method, with a mean bias of -1.3 °C and -2.0 °C, respectively. Its total error is of 2.0 °C RMS, dominated by the bias (2.6 °C for the SC method). The improved single-channel method shows slightly more accurate results, and it is used in the following to evaluate the estimation of snow surface temperature by the modelling chain.

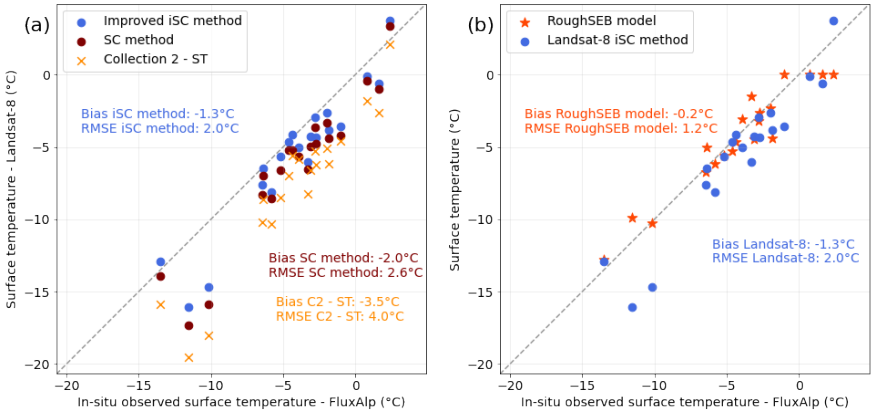

Figure 5. Landsat-8 retrieved surface temperature as a function of surface temperature measurements at FluxAlp station. In **(a)** using the iSC method (blue) and the SC method (brown), Collection 2 Surface Temperature product (orange); in **(b)** simulated T_s by the model (red) and observed T_s by Landsat-8 (iSC method – blue). The 1:1 dashed line represents perfect agreement with in situ measurements.

3.2 Snow surface temperature simulations

3.2.1 Validation at FluxAlp station

Figure 5b shows Landsat-8 observations and snow surface temperature simulations, compared to the in situ measurements at FluxAlp. The RoughSEB model is in general in agreement with the satellite observations. Considering all ~~20 scenes~~the images, they differ by ~~only 0.1~~up to 1 °C, the simulations being slightly warmer. The differences are however larger when considering the coldest cases, up to 5 °C. The error of the simulations is lower, of ~~1.5~~1.2 °C RMS (2.0 °C for Landsat observations). ~~The estimation of T_s at this particular point is therefore accomplished for a variety of weather conditions and solar zenith angles.~~

3.2.2 Evaluation of the diurnal cycle

The modelling chain to estimate T_s is evaluated over a diurnal cycle at the FluxAlp station (Fig. 6). A period of ≈ 36 h was selected after one of the Landsat-8 acquisition dates, starting at ~~9h~~ 9:00 UTC on 10 March 2016. This period featured stable conditions and the sky was clear, except for a few minutes at the end of the period. Figure 6 (top) shows the temporal evolution of the radiative fluxes (SW_{net} and LW_{net}) and the turbulent fluxes (sensible heat flux H and latent heat flux L). The simulations are run hourly, with a constant SSA = 20 $m^2 kg^{-1}$ and aerodynamic roughness length $z_0 = 10^{-3}$ m. ~~They~~ The radiative fluxes are compared to the in situ measurements at the station, ~~except in the case of the~~ and the simulated turbulent heat fluxes ~~, which are as well simulated from the measured wind speed, air temperature and humidity – from that the notation: in situ derived~~are shown for completeness. It should be recalled that the simulations are run with a spectral range 300 - 4200 nm for the SW in order to cover all the solar radiation spectrum. However, for a fair comparison with the measured SW_{net}, additional SW calculations are run in the same spectral range of the pyranometer (300 - 2800 nm). As measurements at ~~FluxAlp site~~ the

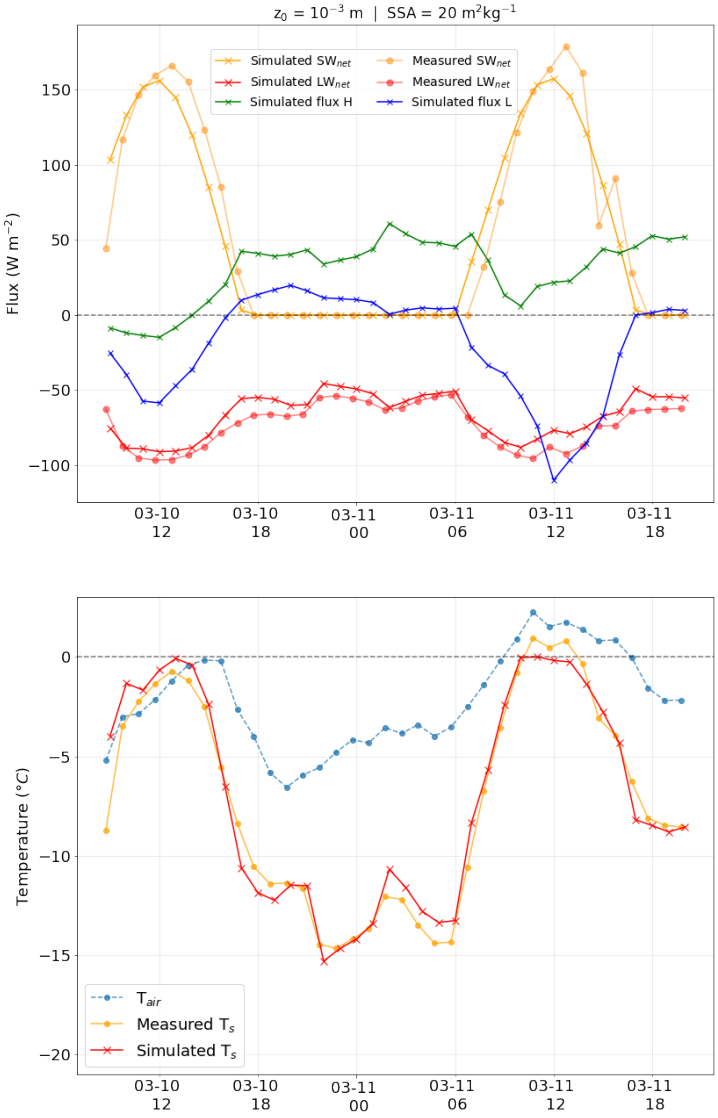

Figure 6. Simulation of the ~~terms of the~~ surface ~~energy budget~~ fluxes (top) and snow surface temperature (bottom) at the FluxAlp station for a ≈ 36 h long time series ~~on~~ starting 10 March 2016. ~~They~~ The radiative fluxes are compared to in situ measurements~~(except *H* and *L* fluxes which are also estimated from the measurements)~~. All times are in UTC.

405 FluxAlp station are averaged over the preceding 30 minutes, a 15 min time shift is applied on the graph~~for a fair comparison~~. The results show that the net short-wave flux is slightly underestimated except during the first hours of sunlight when it is overestimated. The difference is ~~small~~ almost negligible (< ~~20~~5 Wm^{-2}) around ~~10h-10h30~~ 10:00-10:30 UTC, which by chance corresponds to the Landsat-8 acquisition time. The underestimation leads to an overall bias ~~during~~ over daytime of ≈

~~15~~5 $\mathrm{Wm^{-2}}$, while the net long-wave radiation flux is in general overestimated by $\approx$ ~~10~~7 $\mathrm{Wm^{-2}}$. ~~The turbulent fluxes are well simulated compared to the values estimated at FluxAlp site. It is worth recalling that both heat fluxes are calculated using the same equation and assumptions, which limits the strength of this result.~~ Figure 6 (bottom) shows the evolution of the simulated T_s over the same period, compared to the in situ measurements. Observed air temperature is also shown for completeness. There is a good agreement between the simulations and the measurements, within ~~-0.3~~0.2 °C (RMSE: ~~0.9~~0.8 °C). Surface temperature shows a ~~remarkable~~ diurnal cycle, where the melting point is ~~almost~~ barely reached in the early afternoon, and the lowest temperatures are reached at night~~, in the absence of solar radiation. The~~ . The bias in T_s towards the end of the afternoon could be explained by the balance between the underestimation of the net SW flux ~~(and therefore the energy absorbed in the snowpack) and the~~ and the overestimation of the net LW flux~~could explain the bias obtained in the snow surface temperature in the morning and at the end of the afternoon~~. The slight variations in surface temperature (around 2 to 3 °C) during the night are mainly driven by the balance between the long-wave radiation flux and the sensible heat flux, the other fluxes being negligible.

3.2.3 Evaluation of the spatial variations

To evaluate the spatial variations of T_s, the simulation corresponding to the Landsat-8 acquisition on 18 February 2018 is analysed here. It is chosen because in situ SSA measurements were available (Tuzet et al., 2020), allowing a more ~~effective assessment~~ accurate estimate of the surface albedo. The SSA value is 45 $\mathrm{m^2 kg^{-1}}$.

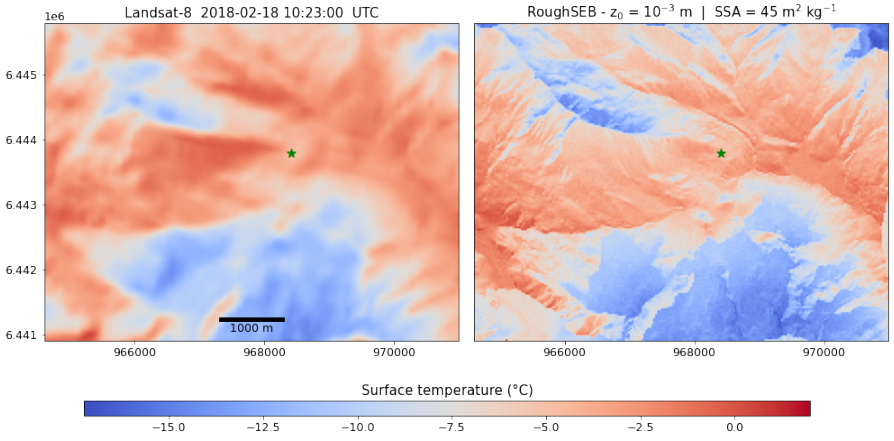

Figure 7. Surface temperature observed by Landsat-8 (left) and simulated by the RoughSEB model (right) in the Col du Lautaret area on the 18 February 2018. The location of the FluxAlp station is highlighted by the green marker. Projection is Lambert 93 (EPSG: 2154) and the coordinates are in meters.

Figure 7 shows the spatial variations ~~in~~ of snow surface temperature, observed by Landsat-8 (left) and simulated by the RoughSEB model (right). The variations are well represented by the model, with many similarities at all the scales across the ~~scene~~domain. The small-scale variations are better resolved by the model as ~~its~~ the spatial resolution is significantly higher (10 m vs 30 m for the satellite). This is in particular true in the northern area of the ~~scene which covers~~ domain which features a

series of small valleys, showing a larger temperature gradient in the simulation. The model is slightly colder in the coldest areas (e.g. shadows in the southern area of the scene), as well as in the warmest areas around the FluxAlp station (green marker). As showed in Fig. 5b, the surface temperature does not differ significantly in the FluxAlp area.

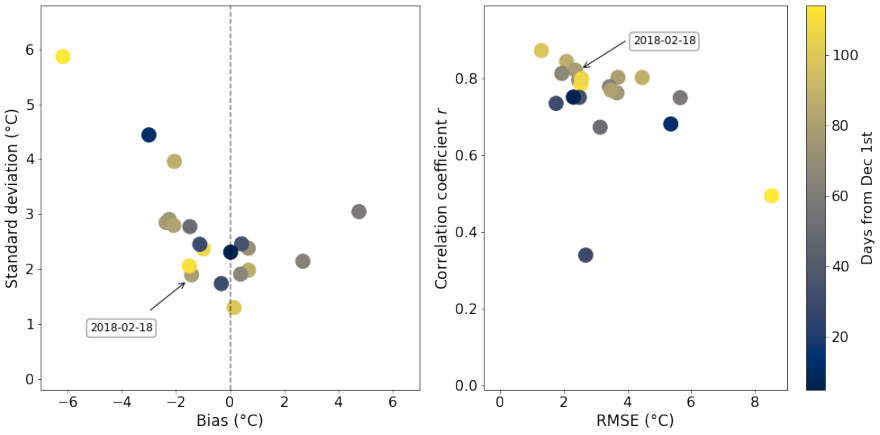

Figure 8. ~~Mean bias and standard deviation~~ Comparison of the spatial variations of surface temperature between the simulations and the satellite observations for each date, computed considering the whole ~~area~~domain. ~~The simulation on 18 February 2018 presented in Fig~~On the left, mean bias and standard deviation of the differences. ~~7 is highlighted by~~ On the ~~rounded marker~~right, the RMSE and the correlation coefficient r.

Figure 8 (left) shows the bias and standard deviation of a pixel-to-pixel comparison between all the 20 satellite observations and the corresponding simulations. The latter are resampled to 30 m to match the spatial resolution of the Landsat-8 observations. Figure 8 (right) shows the correlation coefficient r as a function of the RMSE between simulations and remote sensing observations. The simulations are slightly colder in general, with a ~~negative bias comprised principally between -4~~bias principally between -3 °C and ~~0~~1 °C. ~~Some simulations are however warmer than the satellite observations.~~ The standard deviation of the ~~difference~~ differences varies mostly between 1 and 3 °C (2 and 4 °C ~~. The~~ for the RMSE). Some outliers are observed, and in particular the simulation that shows the highest differences (both standard deviation and RMSE) corresponds to an acquisition from late March~~2019.~~. Such differences could be explained with an early onset of snowmelt (snow patches in the lowest areas) due to mild temperatures, a particular situation that ~~is not yet correctly resolved by the model. Nevertheless,~~ breaks the assumptions in the model (e.g. 100% snow cover). The shallow snowpack in early winter (probable patches of bare soil) can lead to a similar situation, where the bare soil temperature would be certainly different than that of snow-covered terrain. This could explain the lowest correlation value of the dataset which corresponds to an acquisition from early December. Nevertheless, apart from these two cases, considering all acquisitions, these differences ~~don't~~ do not seem to be clearly related to the time of the year (~~i. e. early or late winter~~shown as color in Fig. 8), so strong conclusions cannot be drawn.

~~This~~ These results show the performance of the RoughSEB model to simulate the snow surface temperature ~~and the surface energy budget~~ in complex terrain within a reasonable accuracy. ~~Their~~ The temporal and spatial variations of T_s are also well

represented in the study area. To understand these variations, the role of the topographic effects ~~that govern them~~ is addressed in the following section.

3.2.4 Relative importance of the topographic effects

In order to quantify the relative importance of the topographic effects, we ~~have~~ run a series of simulations where every effect considered in this work is disabled at a time. The importance of applying an elevation-corrected downward LW flux instead of considering a uniform one is also quantified. Figure 9 shows the impact on the surface temperature distribution across the area ~~for~~ on the 18 February 2018. The scatter plots show the modelled T_s for every pixel in the ~~area~~ domain as a function of the T_s ~~observed by Landsat-8~~from the reference simulation (REF), where all the effects are included. The histogram plots show the distribution of all the pixels and in addition, the reference simulation (black line) – including all the effects – and Landsat-8 observations (red).

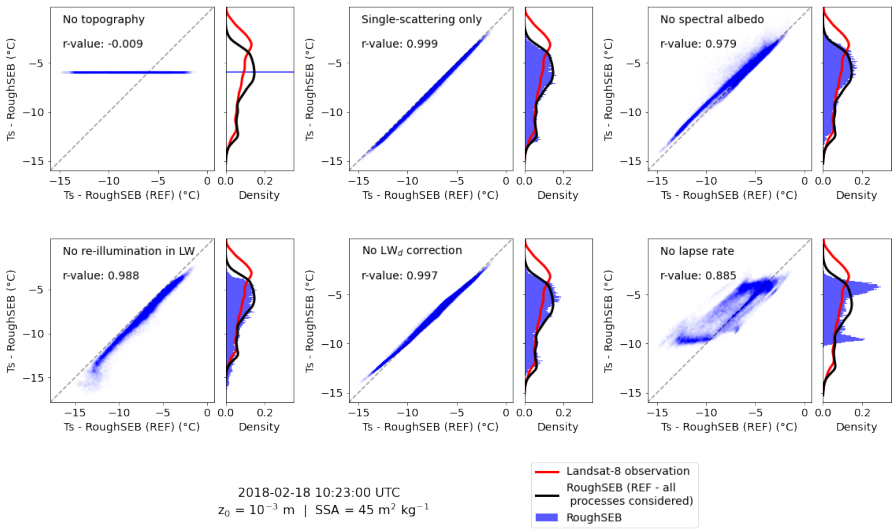

Figure 9. ~~The~~ Impact of disabling a topographic effect on the simulated T_s on 18 February ~~2018 as a function of the observed T_s by the satellite.~~ 2018. Every single panel ~~correspond~~ corresponds to a disabled topographic effect~~disabled~~, with respect to the reference simulation (REF) where all ~~processes~~ the effects are ~~considered~~included. The marginal histograms show the distribution of surface temperature for each ~~simulations~~ simulation as well as the observed T_s by the satellite (red) and the reference simulation (black).

To extend these results to all the dates, Fig. 10 displays summary statistics of the difference between the simulations with a disabled topographic effect and the reference simulation. The left panel presents the mean difference between the simulation without the effect and the reference simulations (for each effect) while the standard deviation of the differences (right panel) shows how both simulations agree in terms of spatial variations. A value close to zero means that the effect is negligible in terms of average and variations respectively.

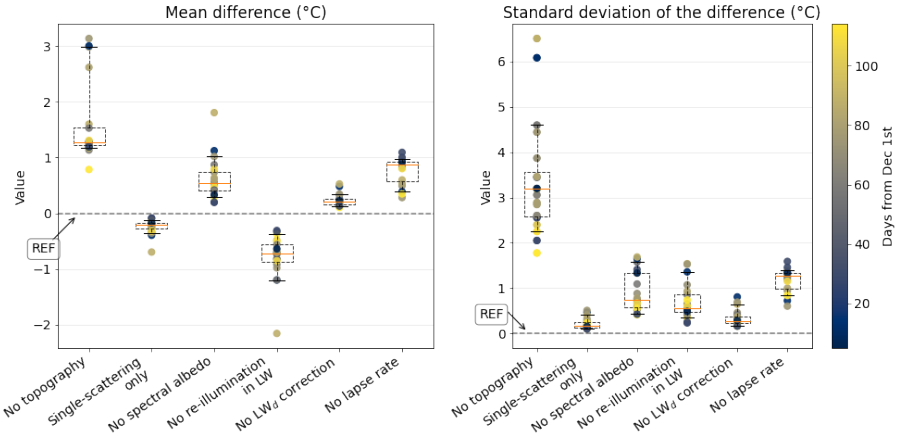

Figure 10. Overall representation of the mean difference and standard deviation between the reference simulation (REF), where all processes are considered, and the additional simulations where one topographic effect is disabled at a time. The whiskers of the boxplots represent the 10th and 90th percentiles of the distribution.

When no topography is taken into account (i.e., a perfectly flat surface instead of the actual topography), the snow surface temperature is uniform (~~-6.9~~-5.9 °C) across the scene. This value overestimates the mean temperature of the reference simulation (~~-7.9~~-7.2 °C), showing that not only the spatial variations of temperature are not represented (r-value ≈ 0), but even on average a simulation ~~on a~~ with flat terrain is not equivalent to the mean temperature of the area with topography. This ~~basic~~ simulation highlights the considerable effect of the topography on the surface temperature and the importance to take it into account even for large scale simulations. Considering all the 20 dates, neglecting the topography results in an overall overestimation of ~~1.0~~1.3 °C (median value) and the standard variations with respect to the reference simulation are high with a median value of ~~2.5~~3.2 °C and a maximum of ~~5~~6 °C.

The simulation with single-scattering only in the SW, (only the first bounce of the photons is considered by RSRT, ~~multiple scattering~~ the absorption enhancement is neglected) shows very small differences with respect to the reference simulation. It is only slightly colder, in particular in the coldest pixels. This is mainly due to neglecting the ~~re-illumination caused by multiple bouncing~~ illumination in the shadowed (and cold) areas coming from other facing slopes. Nevertheless, the impact is not significant, the mean difference being ~~of~~ barely different from zero (median of -0.2 °C, standard variations of ~~0.1~~0.2 °C). The smallest impact is observed in ~~December~~ early winter which could be explained by a dependence on the solar zenith angle, and on how the topography modulates the received solar irradiance. Overall, this result means that, at least in our study area, the absorption enhancement caused by multiple bouncing is almost negligible.

When neglecting the spectral dependence of snow albedo and thus ~~considering only~~ calculating SW_{net} directly from the broadband albedo (≈ 0.87 on 18 February 2018), the simulated surface temperature is slightly warmer than the reference with overall differences of ~~0.4~~0.5 °C (median of the means) and of ~~0.6~~0.7 °C (median of standard deviations)~~and~~ , with a maximum beyond ~~1~~1.5 °C. This shows the importance of taking into account this effect involving the coupling between spec-

tral dependence of snow albedo and ~~topographic effect is important to take into account, as it plays a role that needs to be considered~~topography.

The effect of the thermal emission by surrounding terrain in the LW is obtained by estimating the surface temperature as if the terrain was flat (first step as detailed in Sect. 2.1.2). ~~The~~ For the selected date in Fig. 9 the peak of the distribution is less marked and widened in the range (-5 °C – -8 °C), and ~~the impact is a systematic underestimation of~~ T_s ~~. This is true for~~ is systematically underestimated when this approximation is applied. The difference in the warmest areas of the ~~scene (higher than~~ domain (≥ - 5 °C) ~~where the underestimation is of -0.7~~is of -0.6 °C~~, and in particularly true for~~ . In the coldest areas (~~lower than~~ < -12 °C), ~~with an underestimation of -1.2~~the underestimation is of -1.4 °C~~. In the latter,~~ , because direct radiation is absent and the ~~radiative~~ radiation budget is dominated by diffuse and weak illumination. The thermal emission by surrounding faces warms these cold areas as a function of their sky-view factor. The mean difference ~~goes down to -0.6~~is -0.7 °C (standard variations of ~~0.4~~0.6 °C) when considering all the ~~scenes~~simulations.

Neglecting the altitudinal variations of the downwelling LW flux over the study area has a limited impact on T_s. Slight differences are mainly concentrated in the range (-3 °C – -8 °C) and also in the coldest areas, where the T_s is overestimated by almost 0.6 °C. Part of these zones are at the highest altitudes of the study area, and without the correction they receive more downwelling LW flux (up to ≈ 15-20 $\mathrm{Wm^{-2}}$), leading to warmer surface temperature. Overall, neglecting the altitudinal variations barely overestimates the estimation of T_s by 0.2 °C, with errors that are not significant (median value of 0.3 °C).

With respect to the altitudinal variations of air temperature (lapse rate effect), the distribution shape squeezes and even becomes bimodal, with two marked peaks at -5 °C and -10 °C ~~. The difference~~ when the lapse rate is neglected (Fig. 9). The differences to the reference simulation ~~is~~ are significant when considering all the dates, with a median value of 0.9 °C and a median standard deviation of 1.3 °C. Introducing the lapse rate effect tends to warm the air on the lower parts of the ~~scene~~ domain (usually the ~~warmer~~warmest) and the opposite on the ~~higher and colder~~ highest and coldest facets. Since the FluxAlp measurement station (where the reference air temperature is taken) is in the lower range of altitudes of the study area the overall impact of neglecting the lapse rate effect is an overestimation (0.9 °C). This result is specific to ~~our setting~~ the position of the station with respect to the altitudinal distribution and using a different reference air temperature would change this result. ~~In principle it is possible to choose the reference at the mean altitude of the area which leads to a null bias. Nevertheless~~On the contrary, the standard variations are also significant and this is not specific to our setting. It effectively shows that neglecting the altitudinal variations of air temperature results in an overall significant error of 1.3 °C (median) in surface temperature over the study area. The correlation coefficient is the lowest, with a median value of 0.921 considering all the simulations.

~~Theses results gives~~ These results give the relative importance of the topographic effects investigated here. Neglecting the topography (i.e. assuming a flat surface) is ~~, as expected ,~~ as expected the most important source of error when simulating snow surface temperature. Neglecting the altitudinal variations of air temperature ~~(lapse rate effect)~~ is the second effect in terms of importance. It is followed by the thermal emission by surrounding terrain in the LW and the spectral dependence of snow albedo, the latter being slightly less important. Finally, the absorption enhancement caused by multiple bouncing is almost negligible, as well as taking into account the altitudinal variations of downwelling LW flux.

4 Discussion

4.1 Retrieval of surface temperature from satellite observations

The assessment of our modelling chain was performed against in situ and satellite observations, the latter being crucial for the spatial variations. However, ~~these~~ they depend on the choice of the method for the atmospheric correction. Here we implemented two single-channel methods for Landsat-8 thermal imagery: the SC method (Jiménez-Muñoz and Sobrino, 2003), and the iSC method (Cristóbal et al., 2018) and we compared them to the recent Surface Temperature product. The iSC method is the most accurate (within $\approx 1\,°C$) at the FluxAlp measurement station. The Collection 2 Surface Temperature product is the less accurate (within 3.5 °C). However, this does not preclude of the quality in the whole area. In particular, we assumed that the whole scene is covered by snow, with an emissivity equal to 0.98. However, in alpine areas, vertical mountain ridges or patches without snow on sun-facing slopes are frequent and may ~~results in more~~ result in a variable emissivity over the scene. A possible future improvement would be to ~~consider an emissivity mask , where each pixel would have a particular value~~ include a land mask to set a particular emissivity value for each pixel depending on the presence of snow, rocks, grass, etc. This is normally achieved by means of NDVI-based classifications (Li et al., 2013) that can be adapted to snow-covered complex terrains with methods that rely on the snow cover area (Varade and Dikshit, 2020). The Surface Temperature product~~(which is already generated using this method) presents worse results at our validation point, but overall, ~~, which includes NDVI-based classifcations, is less accurate than the methods without this refinement (at the FluxAlp station). Overall, the differences across the study area between the iSC method and this official product are of 0.3 °C (median of standard deviations)~~considering the whole dataset~~, which is considerably lower than the difference at FluxAlp. The satellite thermal observations from Landsat-8 are therefore correct enough to assess the model performance, with an accuracy of the order of 1 °C and a precision lower than 0.5 °C.

4.2 Snow surface temperature estimation

~~One question that arises is about the performance of the model to estimate the T_s and its temporal and spatial variations in complex terrain.~~ The simulations show an overall agreement with both in situ measurements and satellite observations (Sect. 3.2). The simulated fluxes ~~to be considered in the surface energy budget~~ and the temporal evolution of T_s are well represented for a daily cycle (Fig. 6). The net SW flux is slightly underestimated during ~~most~~ part of the day (except in the ~~early~~ morning when it is slightly overestimated), but the impact on surface temperature is balanced by the other terms of the energy budget~~, in particular due to the slight overestimation of the net LW flux. The~~ . The treatment of the turbulent heat fluxes ~~are essential for an accurate calculation of the surface energy balance, in particular during the night, when they balance the LW radiation flux. Their treatment in the model~~ in the model at this stage is very simple~~,~~ : the atmosphere is assumed neutral, the aerodynamic roughness length is uniform, the wind is uniform, etc. Some of these simplifications are required ~~to achieve good~~ for the computational performances and may be challenging to take into account ~~(wind field)~~ while others (e.g. atmospheric stability) could be easily implemented (Essery and Etchevers, 2004).

The ground heat flux was also neglected~~meaning~~, which means that the surface temperature reacts immediately to changes of the downwelling radiation. In reality, the snowpack has some thermal inertia which delays and moderates the diurnal amplitude of T_s~~, resulting in~~. If significant, this would lead to an overestimation in the morning and underestimation in the late afternoon, when the ~~cooling~~ warming (cooling) of the surface is more pronounced in the simulations as the solar zenith angle ~~increases~~decreases (increases). Nevertheless, this delay is barely visible in our case (Fig. 6). Snow is indeed a highly insulating ~~medium~~ material and has a small thermal inertia. ~~With~~ Assuming a thermal conductivity of around $0.2\,\mathrm{Wm^{-1}K^{-1}}$ (Sturm et al., 1997), the daily wave penetrates by no more than $20\,\mathrm{cm}$ ~~in~~ into the snowpack. It means that with a diurnal cycle half-amplitude of $\approx 7\,^{\circ}\mathrm{C}$ in surface temperature, the maximum temperature gradient in the upper snowpack is of the order of $35\,\mathrm{Km^{-1}}$. According to the Fourier law, this implies a maximum ground heat flux $G \approx 7\,\mathrm{Wm^{-2}}$ which is an order of magnitude lower than the radiative and turbulent heat fluxes estimated in our case (Fig. 6). This simple calculation confirms that neglecting G is acceptable in a first approximation when snow is relatively fresh and is not melting. In spring, with a denser and less insulating snowpack and with melt, this approximation needs to be reconsidered. However, taking into account the thermal diffusion in the snowpack over millions of facets represent a ~~very~~ significant computational cost~~and requires approximations~~.

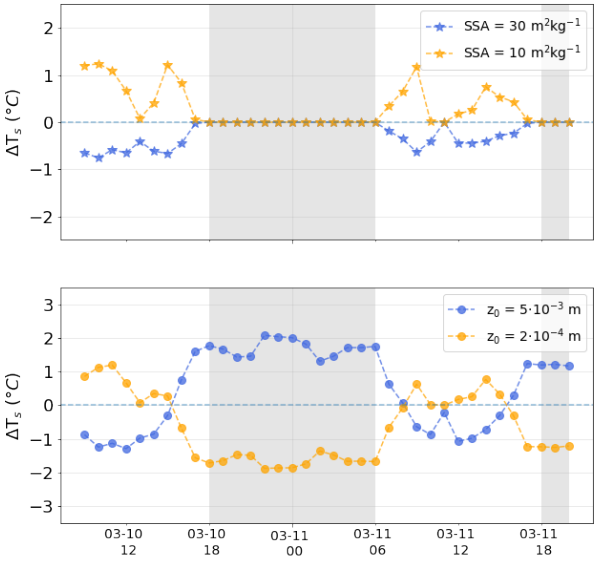

Figure 11. Changes in simulated snow surface temperature (ΔT_s) for a diurnal cycle at the FluxAlp station when varying the specific surface area (SSA – top) and the aerodynamic roughness length (z_0 – bottom). The shaded areas corresponds to night time (i.e. SZA below 0° or over 90°).

The choice of input parameters such as SSA and aerodynamic roughness length (z_0) is critical for the simulations. Local measurements are not always available and may not be representative of the whole area. SSA ~~plays a crucial role on~~ drives the albedo and~~so on~~, in turn, the short-wave absorption by the snowpack. The sensitivity of snow surface temperature to SSA is ~~shown~~ assessed in Fig. 11 (top), for the diurnal cycle presented in Fig. 6. SSA ~~varies in~~ is varied by $\pm\ 10\,\mathrm{m^2kg^{-1}}$ with

565 respect to the reference simulation for the whole time series ($20\,m^2kg^{-1}$). The impact of varying SSA on T_s is up to 1 °C, and is larger when considering a low SSA than a large SSA. This is mainly due to the fact that the relationship SSA-albedo is ~~not linear, as shown by Domine et al. (2006)~~non-linear (Domine et al., 2006). In general, spatio-temporal variations of SSA are expected in our area because the ~~initial~~ fresh snow SSA value depends mainly on snowfall temperature ~~mainly~~ and its subsequent evolution is a general decrease depending on the thermal evolution of the snowpack (Domine et al., 2008). As a
570 result, SSA is expected to be higher at ~~higher~~ the highest altitudes and in the shadows where the conditions are colder~~, and so does the~~. Higher SSA leads to less short-wave absorption, which would tend to increase the cooling in these areas compared to lower SSA areas. ~~This could also~~ The spatial variations of SSA could be modelled, for instance, using SSA retrieved by satellite (e.g. Kokhanovsky et al. (2019)). The temporal variations of SSA could explain the differences between the simulated and measured ~~net short-wave~~ SW_{net} flux, as here the value was kept constant for the whole time series.

575 The aerodynamic roughness length controls the sensible and latent heat fluxes, so it shall also be carefully ~~tuned~~prescribed. In this study, a value of 10^{-3} m is assumed, which is standard according to previous works (e.g. Brock et al. (2006)). The sensitivity of T_s to aerodynamic roughness length is shown in Fig. 11 (bottom). z_0 varies by a factor of 5 with respect to the reference simulation. The choice of z_0 has a ~~more~~ significant impact on the simulated surface temperature, in particular during the night (up to 2 °C), when the SW radiation is absent. ~~Martin and Lejeune (1998)~~ Previous works
580 (Martin and Lejeune, 1998; Kuipers Munneke et al., 2009) found similar variations ~~using the snow model Crocus, with a slightly different approach that considered changes of atmosphere stability, as well as Kuipers Munneke et al. (2009) with even another approach for~~ with different approaches. A different formulation of the turbulent heat fluxes ~~.~~(e.g. atmospheric stability) could lead to smaller differences during the night, in particular with stable conditions. According to Brock et al. (2006), snow z_0 can vary up to three orders of magnitude depending on the time of the season ~~(i.e. early or mid ablation season) and also~~
585 and on snow type (i.e. fresh snow or melting snow). To estimate ~~its~~ the expected spatial variations in a mountainous area of several km^2, a ~~parametrization of SSA evolution~~ parameterization of snow z_0 as a function of the snow type would be possible ~~(Domine et al., 2007) or by using SSA retrieved by satellite (e. g. Kokhanovsky et al. (2019)).~~ via the snow SSA (Domine et al., 2007).

The spatial variations of ~~surface temperature~~ T_s are clearly dependent on the topography and are correctly simulated (Fig.
590 7). They seem to depend ~~in particular~~ on slope orientation, as shown in Fig. 12. For larger slopes (> 30°), the lack of direct radiation governs the surface temperature in some areas, such as the ~~northern~~ north-facing (N-W to N-E) ~~slopes covered in the shadow at the southern part of the scene. The south-facing slopes are more numerous and feature an extended range of surface temperature . The temperature~~ shadowed slopes. The temperature difference is large between opposed slopes (on the order of 5 to 10 °C~~in a few hundred meters~~). Overall, the mean T_s of the ~~northern facets is -10.5~~north-facing facets is -10.7 °C (±
595 ~~1.7~~1.9 °C). They are considerably colder than the southern (S-E to S-W) ones (~~-6.7~~-5.6 °C (± ~~1.5~~1.8 °C)). These differences are consistent with previous studies (e.g. Fierz et al. (2003)), and highlight the necessity of accounting for spatial variations of surface temperature in mountainous areas~~, where larger slopes prevail over gentle terrain~~.

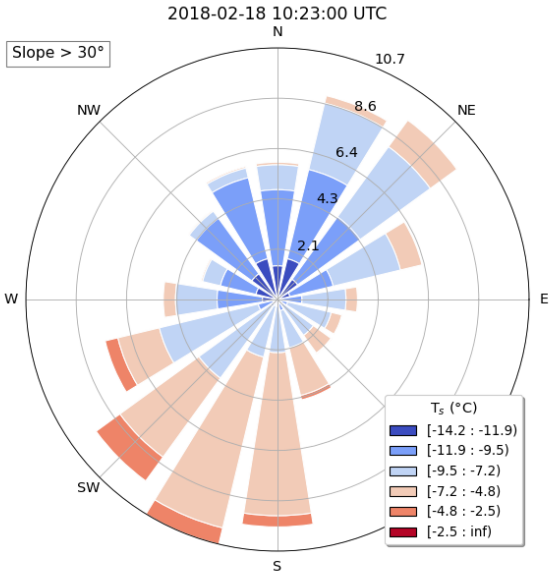

Figure 12. Distribution of simulated surface temperature as a function of the aspect for slopes larger than 30°. The radius of each of the 16 sectors corresponds to the normed (displayed in percent) quantity of facets.

4.3 Role of the topographic effects

The results presented in this study show that the topography controls the ~~energy budget and the~~ surface temperature to a large extent. However modelling all the processes involved in complex terrain ~~may lead to~~ has prohibitive computational cost for most applications. This has an adverse outcome: some of them are usually neglected or approximated. Our modelling chain takes into account a relatively comprehensive set of ~~processes~~effects, especially on the radiative aspects. The motivation of this study is therefore to quantify their relative importance, in order to ~~provide some insight on which one of them~~ determine which ones can be neglected as a function of the targeted accuracy.

The role of the topography is quantified in Sect. 3.2.4, where we compared the reference simulation (where all effects are considered) to simulations where we disabled one effect at a time. Overall, we found that the absence of topography (i.e. terrain altitude, slope and aspect), and therefore the presence of ~~altitudinal variations~~ variations in altitude and self and cast shadows is the most important effect. Errors of several °C are to be expected if considering a flat surface. The same conclusion is drawn by Yan et al. (2016) which found significant errors in the estimation of net LW radiation flux by assuming a flat surface at a larger scale over the Tibetan Plateau.

Yan et al. (2016) also accounted for the sky-view factor and the contribution of thermal radiation coming from surrounding terrain. Our results show a cooling effect of ~~mean difference of~~ almost 1 °C (median of ~~-0.6~~-0.7 °C) when disabling these two topographic effects. This agrees with the results presented by Arnold et al. (2006), showing a similar ratio of importance

between the ~~role of the~~ shadows and the LW contribution when considering glacier melt. To take into account this effect, the downwelling LW radiation flux in each facet is updated with the thermal emission of the surrounding facets, which is derived ~~with~~ from an average T_s ~~for~~ over the whole scene. Such an approximation saves a lot of computation time but, as a result, the differences in thermal emission due to spatial variations of surface temperature are masked. ~~The warmest facets will~~ In reality, the warmest facets emit more LW radiation than the coldest ones, leading to spatial differences in the ~~modelled~~ T_s. Neglecting the variations in altitude of the downwelling LW flux has a lower influence on surface temperature. For the selected simulation (Fig. 9), the elevation-corrected flux spans from 180 to 213 $\mathrm{Wm^{-2}}$, while the measured flux is 204 $\mathrm{Wm^{-2}}$. This range is consistent with other works (Greuell et al., 1997; Iziomon et al., 2003), and the impact on T_s is only significant (> 0.5 °C) in the coldest areas.

Our results show a significant impact on the simulated T_s ~~by~~ when disabling the altitudinal variations of air temperature, with a warming effect up to 1 °C. The spatial and temporal distribution of air temperature, as well as wind dynamics in mountainous areas, have been widely investigated (Jiménez and Dudhia, 2012; Rotach et al., 2015)~~, and different~~. Different parameterization and estimation methods exist to overcome ~~its~~ their complexity (e.g. Wood et al. (2001)). The approach implemented here is simple, with several approximations and ~~important assumptions~~ rough assumptions (as a constant aerodynamic roughness length and wind speed across the study area). Future improvements of our approach could benefit from wind downscaling methods to better represent wind speed distribution over complex terrain, as in Helbig et al. (2017).

~~Arnold et al. (2006) also pointed out the role of the anisotropic reflectance of snow and ice at high solar zenith angles. This is found to be essential to correctly estimate the radiative budget. The RSRT model can account for this effect (Larue et al., 2020) but we did not consider it here. The reason is that we preferred to account for~~ This study accounts for the spectral dependence of snow albedo, which is an improvement with respect to most of the models that only account for broadband albedo. ~~The impact in T_s is however limited, but errors up to ≈ 1 are possible.~~ As running RSRT at many wavelengths is very expensive, we developed the effective method present in Eqs. 5 and 6. ~~Unfortunately, this method relies on the Lambertian approximation which makes it incompatible with taking into account the reflectance anisotropy~~The impact on T_s is limited, but errors up to ≈ 1.5 °C are possible. The relative importance is similar to that of the thermal emission from surrounding slopes, and is not negligible.

~~Another~~ The last topographic effect investigated here is the influence of the multiple bounces of photons between the faces in the short-wave domain, also called re-illumination or cause of absorption enhancement. It is simulated with the RSRT model (Larue et al., 2020) and represents the most expensive step of the modelling chain in terms of computational cost, as each photon is tracked until it escapes the scene, after one or several bounces. ~~Our results~~ The results presented here suggest that the re-illumination can be neglected, with a limited impact on the surface temperature estimations (~~< 0.3~~ < 0.2°C). This implies that RSRT is only needed to track the shadows, slope and compute the sky view factor. In principle these effects can be taken into account by other faster methods (e.g. Dozier et al. (1981)). Nevertheless, other authors have drawn different conclusions regarding the role of re-illumination in the same study area. Lamare et al. (2020) found a significant contribution of multiple reflections on the simulated TOA radiance in ~~rugged terrain~~the same area as ours. An hypothesis to explain this discrepancy is the dependence on the sun's position and the configuration of the terrain. Earlier simulations in the winter season (closer

to December 1st) show a lower impact than later ones. However, this point requires further investigation~~to derive stronger conclusions~~, in particular as atmospheric scattering and absorption effects due to the air within the relief are neglected in the present work.

5 Conclusions

We have investigated the relative importance of several topographic effects in a mountainous terrain in the French Alps. For this, we have first developed a ~~chain of models~~ modelling chain to predict surface temperature, ~~by~~ combining existing radiative transfer models (RSRT, SBDART) and a new surface energy budget model (RoughSEB). This chain ~~has been~~ was evaluated against in situ measurements and remote sensing thermal observations to account for the spatial variations. ~~The latter have been corrected for atmospheric effects with a single-channel algorithm.~~

A $\approx$ 36 h long time series was simulated and an overall agreement is achieved with the in situ measurements, within ~~0.3~~0.2 °C. Besides, the bias of the simulations at the FluxAlp station for the 20 scenes corresponding to the Landsat-8 acquisitions is only ~~-1.2~~-0.2 °C (total error of ~~1.5~~1.2 °C RMS), which highlights the potential of the chain to simulate surface temperature within a reasonable accuracy and precision. The spatial variations across the 50 km^2 scene are also well represented, with ~~a standard deviation of the~~ differences to the satellite observations ~~comprised between 2~~ mainly comprised between 1 and 3 °C, which is small compared to the actual surface temperature variations of 5-10 °C between the slopes in the study area.

~~A few topographic effects that are~~ The topographic effects responsible for such spatio-temporal variations ~~have been investigated and their relative importanceis~~are ranked by order of importance: 1) ~~The~~ the modulation of solar irradiance by the terrain slope and aspect (i.e. the presence of topography), 2) the altitudinal changes in air temperature (lapse rate effect), 3) the contribution of thermal radiation coming from surrounding terrain, 4) the spectral dependence of snow albedo, ~~and~~ 5) the changes in downward long-wave flux because of variations in altitude, and 6) the absorption enhancement caused by multiple bouncing of photons in the SW domain. ~~Their importance has been quantified and the warming (or cooling) effects are up to 1 , except for the first one (absence of topography) that lead to errors of several degrees Celsius in surface temperature.~~

~~The modelling chain shows some limitations justified by the assumptions made on some of the parameters controlling the radiative budget, such as snow SSA or the aerodynamic roughness length z_0. Nevertheless, it shows good performance to estimate snow surface temperature and its spatial variations, and has several applications. It allows a better understanding of the processes that govern the surface energy budget in snow-covered, mountainous areas. A first~~ A future possible extension of the ~~model is to investigate the snowmelt . Another~~ modelling chain should aim at investigating snowmelt and patchy snow conditions. An application is the preparation ~~, and in the future the calibration/validation~~ of the thermal infrared TRISHNA satellite mission (Lagouarde et al., 2019) ~~which~~ and in the future its calibration/validation. TRISHNA will provide from 2025 high resolution images (50 m) of the Earth surface temperature in mountainous areas with a 3-day revisit time.

Appendix A: Additional equations and mathematical developments

A1 Snow spectral albedo in the Asymptotic Radiative Transfer (ART) theory

The direct and diffuse components of the snow spectral albedo are computed using the ART theory (Kokhanovsky and Zege, 2004). ~~Provided several assumptions about the snowpack (~~We assume that the snowpack is semi-infinite, ~~vertical and horizontal homogeneous layers) and the surface (~~and the surface is flat and smooth ~~–~~ (facets are small enough to be considered as it), ~~they~~ The albedos are expressed as follows:

$$\alpha_{\mathrm{dir}}(\lambda,\theta_{\mathrm{s}}) = \exp\left(-\frac{12(1+2\cos\theta_{\mathrm{s}})}{7}\sqrt{\frac{2B\gamma(\lambda)}{3\rho_{\mathrm{ice}}\mathrm{SSA}(1-g)}}\right) \tag{A1}$$

$$\alpha_{\mathrm{diff}}(\lambda) = \exp\left(-4\frac{\sqrt{2B\gamma(\lambda)}}{3\rho_{\mathrm{ice}}\mathrm{SSA}(1-g)}\right) \tag{A2}$$

where θ_{s} is the solar zenith angle, SSA is the snow specific surface area, ρ_{ice} = 917 kgm^{-3} is the bulk density of ice at 0 °C, $\gamma(\lambda)$ is the ice absorption coefficient ~~(from Picard et al. (2016))~~ (Picard et al., 2016) and B and g are the shape coefficients of snow ~~, taken from Libois et al. (2014)~~(Libois et al., 2014).

A2 Surface exchange coefficient

The surface exchange coefficient involved in the calculation of the turbulent heat fluxes is given by:

$$C_{\mathrm{H}} = 0.16\left[\ln(\frac{z_{\mathrm{t}}}{z_0})\ln(\frac{z_{\mathrm{w}}}{z_0})\right]^{-1} \tag{A3}$$

where z_t and z_w are the ~~height~~ heights at which air temperature and wind speed are measured respectively, and z_0 is the aerodynamic roughness length. Their values are provided in Table B1.

A3 General solution ~~to~~ of the quartic equation~~for $\mathrm{T_s}$~~

The simplified surface energy budget equation ~~eventually become~~ Eq. (14) eventually becomes a quartic equation ~~for~~ with $\mathrm{T_s}$ ~~of the form~~as the unknown:

$$a\,T_{\mathrm{s}}^4 + d\,T_{\mathrm{s}} + e = 0 \tag{A4}$$

where a, d, e are ~~a constant (~~constant for each facet~~)~~. The general solution ~~can be calculated using~~of this equation requires a simple change of variable to transform the quartic into a depressed quartic:

$$T_{\mathrm{s}}^4 + p\,T_{\mathrm{s}}^2 + q\,T_{\mathrm{s}} + r = 0 \tag{A5}$$

which can be solved by means of the Ferrari solution (Neumark, 1965). It consists in adapting the equation to present it as a difference of two squares, which eventually leads to a resolvent cubic that is then solved, yielding:

$$T_s = -S + \frac{1}{2}\sqrt{-4S^2 + \frac{q}{S}} \tag{A6}$$

~~where~~ where q is the simplified first degree coefficient of the depressed quartic equation ($q = d/a$) and where

$$qS = \frac{d}{a}\frac{1}{2}\sqrt{\frac{1}{3a}\left(Q + \frac{\Delta_0}{Q}\right)} \tag{A7}$$

$$\Delta_0 = 12\,a\,e \quad \Delta_1 = 27\,a\,d^2 \quad Q = \sqrt[3]{\frac{\Delta_1 + \sqrt{\Delta_1^2 - 4\Delta_0^3}}{2}} \quad S = \frac{1}{2}\sqrt{\frac{1}{3a}\left(Q + \frac{\Delta_0}{Q}\right)} \tag{A8}$$

with

$$\Delta_0 = 12\,a\,e \tag{A9}$$

$$\Delta_1 = 27\,a\,d^2 \tag{A10}$$

(A11)

A4 Land Surface Temperature retrieval from Landsat 8

LST is calculated for each pixel by applying the radiative transfer equation to a sensor channel ~~, which eventually~~ (Eqs. (1) to (3) in Cristóbal et al. (2018)), which leads to:

$$LST = \gamma \cdot \left[\varepsilon^{-1}\left(\psi_1 \cdot L_{\text{sensor},\lambda} + \psi_2\right) + \psi_3\right] + \delta \tag{A12}$$

where:

$$\gamma = \left\{\frac{c_2 \cdot L_{\text{sensor},\lambda}}{T_{\text{sensor}}^2}\left[\frac{\lambda^4}{c_1}L_{\text{sensor},\lambda} + \lambda^{-1}\right]\right\}^{-1} \tag{A13}$$

$$\delta = -\gamma \cdot L_{\text{sensor},\lambda} + T_{\text{sensor}} \tag{A14}$$

$$T_{\text{sensor}} = \frac{K_2}{ln\left(\frac{K_1}{L_\lambda} + 1\right)} \tag{A15}$$

where ε is the emissivity of the pixel, ψ_i are the atmospheric functions that are parameterized, λ is the effective wavelength (10.904 µm for Band 10), $L_{\text{sensor},\lambda}$ is the top of atmosphere radiance calculated from pixel Digital Numbers (DN) using rescaling factors (USGS, 2021), and T_{sensor} is the brightness temperature in Kelvin. Values of the symbols can be found in Table B1.

The atmospheric functions are statistically fitted from the GAPRI database (Mattar et al., 2015) containing 4714 atmospheric profiles from tropical to arctic atmospheric conditions. The following fit is applied here:

$$\psi_i = i\,w^2 + h\,T_a^2 + g\,w + f\,T_a + e\,T_a^2\,w + d\,T_a\,w + c\,T_a\,w^2 + b\,T_a^2\,w^2 + a \tag{A16}$$

All the coefficient values (from i to a) are in Cristóbal et al. (2018).

Appendix B: Table of symbols

Table B1. Definitions and values of the symbols and magnitudes that appear in this manuscript.

Symbol	Description	Value
σ	Stefan-Boltzmann constant	~~$5.67 \cdot 10^{-8}$~~ $5.67\ 10^{-8}$ $\mathrm{Wm^{-2}K^{-4}}$
$\mathrm{P_s}$	Air pressure	Altitude dependent [Pa]
ρ_{air}	Air density	$\mathrm{P}_s \cdot (287\ \mathrm{T_{air}})^{-1}$ $[\mathrm{kgm^{-3}}]$
$c_{\mathrm{p,air}}$	Heat capacity of air	1005 $\mathrm{Jkg^{-1}K^{-1}}$
L_s	Sublimation heat	2.838~~$\cdot 10^{6}$~~ 10^{6} $\mathrm{Jkg^{-1}}$
z_t	Temperature measurement height	3.53 m - snowdepth [m]
z_w	Wind speed measurement height	5.18 m - snowdepth [m]
z_0	Roughness length	10^{-3} m
c_1	Planck radiation constant	1.19104~~$\cdot 10^{8}$~~ 10^{8} $\mathrm{W\mu m^4 m^{-2} sr^{-1}}$
c_2	Planck radiation constant	1.43877~~$\cdot 10^{4}$~~ 10^{4} μm K
K_1	Landsat calibration constant	774.89 $\mathrm{Wm^{-2}sr^{-1}\mu m^{-1}}$
K_2	Landsat calibration constant	1321.08 K

Appendix C: List of selected Landsat-8 scenes

Table C1. List of selected scenes

Date	Path / Row	Product name
10 February 2015	196 / 029	LC08_L1TP_196029_20150210_20170413_01_T1
19 February 2015	195 / 029	LC08_L1TP_195029_20150219_20170412_01_T1
26 February 2015	196 / 029	LC08_L1TP_196029_20150226_20170412_01_T1
21 January 2016	195 / 029	LC08_L1TP_195029_20160121_20170405_01_T1
9 March 2016	195 / 029	LC08_L1TP_195029_20160309_20170328_01_T1
13 December 2016	196 / 029	LC08_L1TP_196029_20161213_20170316_01_T1
1 January 2018	196 / 029	LC08_L1TP_196029_20180101_20180104_01_T1
2 February 2018	196 / 029	LC08_L1TP_196029_20180202_20180220_01_T1
18 February 2018	196 / 029	LC08_L1TP_196029_20180218_20180307_01_T1
27 February 2018	195 / 029	LC08_L1TP_195029_20180227_20180308_01_T1
22 March 2018	196 / 029	LC08_L1TP_196029_20180322_20180403_01_T1
4 January 2019	196 / 029	LC08_L1TP_196029_20190104_20190130_01_T1
29 January 2019	195 / 029	LC08_L1TP_195029_20190129_20190206_01_T1
5 February 2019	196 / 029	LC08_L1TP_196029_20190205_20190221_01_T1
14 February 2019	195 / 029	LC08_L1TP_195029_20190214_20190222_01_T1
21 February 2019	196 / 029	LC08_L1TP_196029_20190221_20190308_01_T1
18 March 2019	195 / 029	LC08_L1TP_195029_20190318_20190325_01_T1
25 March 2019	196 / 029	LC08_L1TP_196029_20190325_20190403_01_T1
6 December 2019	196 / 029	LC08_L1TP_196029_20191206_20191217_01_T1
31 December 2019	195 / 029	LC08_L1TP_195029_20191231_20200111_01_T1

Author contributions. AR and GP designed the study. GP and FL wrote RSRT, and IO, GP and FL wrote an initial version of RoughSEB. All co-authors contributed to the development of RoughSEB and to the analysis and interpretation of the results. AR prepared the manuscript with contributions of all co-authors.

Competing interests. The authors declare that they have no conflict of interest.

Acknowledgements. This research has been supported by the Centre National d'Études Spatiales (MIOSOTIS and TRISHNA) and the Agence Nationale de la Recherche (ANR-19-CE01-0009 MiMESis-3D). It was also supported by Lautaret Garden – UMS 3370 (Univ. Grenoble Alpes, CNRS, SAJF, 38000 Grenoble, France), a member of AnaEE France (ANR-11-INBS- 0001 AnaEE-Services, Investissements d'Avenir frame) and of the eLTER European network (Univ. Grenoble Alpes, CNRS, LTSER Zone Atelier Alpes, 38000 Grenoble, France). The authors would like to acknowledge staff at Institut des Géosciences de l'Environnement for providing FluxAlp measurements and EBONI team (ANR-16-CE01-0006) for providing SSA measurements.

References

Adams, E., McKittrick, L., Slaughter, A., Staron, P., Shertzer, R., Miller, D., Leonard, T., Mccabe, D., Henninger, I., Catharine, D., Cooperstein, M., and Laveck, K.: Modeling variation of surface hoar and radiation recrystallization across a slope, ISSW 09 - International Snow Science Workshop, Proceedings, 2009.

Adams, E., Slaughter, A., McKittrick, L., and Miller, D.: Local terrain-topography and thermal-properties influence on energy and mass balance of a snow cover, Annals of Glaciology, 52, 169–175, https://doi.org/10.3189/172756411797252257, 2011.

Arnaud, L., Picard, G., Champollion, N., Domine, F., Gallet, J., Lefebvre, E., Fily, M., and Barnola, J.: Measurement of vertical profiles of snow specific surface area with a 1 cm resolution using infrared reflectance: instrument description and validation, Journal of Glaciology, 57, 17–29, https://doi.org/10.3189/002214311795306664, 2011.

Arnold, N. S., Rees, W. G., Hodson, A. J., and Kohler, J.: Topographic controls on the surface energy balance of a high Arctic valley glacier, Journal of Geophysical Research, 111, https://doi.org/10.1029/2005jf000426, 2006.

Arya, S. P.: Chapter 2 Energy Budget near the Surface, in: Introduction to Micrometeorology, edited by Arya, S. P., vol. 42 of *International Geophysics*, pp. 9–20, Academic Press, https://doi.org/10.1016/S0074-6142(08)60417-9, 1988.

Betterton, M. D.: Theory of structure formation in snowfields motivated by penitentes, suncups, and dirt cones, Physical Review E, 63, https://doi.org/10.1103/physreve.63.056129, 2001.

Brock, B. W., Willis, I. C., and Sharp, M. J.: Measurement and parameterization of aerodynamic roughness length variations at Haut Glacier d'Arolla, Switzerland, Journal of Glaciology, 52, 281–297, https://doi.org/10.3189/172756506781828746, 2006.

Brun, E., Martin, E., Simon, V., Gendre, C., and Coléou, C.: An energy and mass model of snow cover suitable for operational avalanche forecasting, J. Glaciol., 35, 333–342, 1989.

Cathles, L. M., Abbot, D. S., Bassis, J. N., and MacAyeal, D. R.: Modeling surface-roughness/solar-ablation feedback: application to small-scale surface channels and crevasses of the Greenland ice sheet, Annals of Glaciology, 52, 99–108, https://doi.org/10.3189/172756411799096268, 2011.

Cathles, L. M., Abbot, D. S., and MacAyeal, D. R.: Intra-surface radiative transfer limits the geographic extent of snow penitents on horizontal snowfields, Journal of Glaciology, 60, 147–154, https://doi.org/10.3189/2014jog13j124, 2014.

Chen, X., Su, Z., Ma, Y., Yang, K., and Wang, B.: Estimation of surface energy fluxes under complex terrain of Mt. Qomolangma over the Tibetan Plateau, Hydrology and Earth System Sciences, 17, 1607–1618, https://doi.org/10.5194/hess-17-1607-2013, 2013.

Corripio, J. and Purves, R.: Surface energy balance of high altitude glaciers in the central Andes: the effect of snow penitents, in: Climate and hydrology of mountain areas, edited by De Jong, C., C. D. and Ranzi, R., pp. 15–27, Wiley, 2005.

Cristóbal, J., Jiménez-Muñoz, J., Prakash, A., Mattar, C., Skoković, D., and Sobrino, J.: An Improved Single-Channel Method to Retrieve Land Surface Temperature from the Landsat-8 Thermal Band, Remote Sensing, 10, 431, https://doi.org/10.3390/rs10030431, 2018.

Domine, F., Salvatori, R., Legagneux, L., Salzano, R., Fily, M., and Casacchia, R.: Correlation between the specific surface area and the short wave infrared (SWIR) reflectance of snow, Cold Reg. Sci. Technol., 46, 60–68, https://doi.org/10.1016/j.coldregions.2006.06.002, 2006.

Domine, F., Taillandier, A. S., and Simpson, W. R.: A parameterization of the specific surface area of snow in models of snowpack evolution, based on 345 measurements, J. Geophys. Res., 112, https://doi.org/10.1029/2006JF000512, 2007.

Domine, F., Albert, M., Huthwelker, T., Jacobi, H. W., Kokhanovsky, A. A., Lehning, M., Picard, G., and Simpson, W. R.: Snow physics as relevant to snow photochemistry, Atmos. Chem. Phys., 8, 171–208, https://doi.org/10.5194/acp-8-171-2008, http://www.atmos-chem-phys.net/8/171/2008/, 2008.

Dozier, J., Bruno, J., and Downey, P.: A faster solution to the horizon problem, Computers & Geosciences, 7, 145–151, https://doi.org/10.1016/0098-3004(81)90026-1, 1981.

Duguay, C. R.: Radiation Modeling in Mountainous Terrain Review and Status, Mountain Research and Development, 13, 339, https://doi.org/10.2307/3673761, 1993.

Dumont, M., Arnaud, L., Picard, G., Libois, Q., Lejeune, Y., Nabat, P., Voisin, D., and Morin, S.: In situ continuous visible and near-infrared spectroscopy of an alpine snowpack, The Cryosphere, 11, 1091–1110, https://doi.org/10.5194/tc-11-1091-2017, 2017.

Essery, R. and Etchevers, P.: Parameter sensitivity in simulations of snowmelt, J. Geophys. Res., 109, 20 111–+, https://doi.org/10.1029/2004JD005036, 2004.

Fierz, C., Riber, P., Adams, E. E., Curran, A. R., Föhn, P. M., Lehning, M., and Plüss, C.: Evaluation of snow-surface energy balance models in alpine terrain, Journal of Hydrology, 282, 76–94, https://doi.org/10.1016/S0022-1694(03)00255-5, 2003.

Filhol, S. and Sturm, M.: Snow bedforms: A review, new data, and a formation model, J. Geophys. Res. Earth Surf., 120, 1645–1669, https://doi.org/10.1002/2015jf003529, 2015.

Gallet, J.-C., Domine, F., Zender, C. S., and Picard, G.: Measurement of the specific surface area of snow using infrared reflectance in an integrating sphere at 1310 and 1550 nm, The Cryosphere, 3, 167–182, https://doi.org/10.5194/tc-3-167-2009, 2009.

Greuell, W., Knap, W. H., and Smeets, P. C.: Elevational changes in meteorological variables along a midlatitude glacier during summer, Journal of Geophysical Research: Atmospheres, 102, 25 941–25 954, https://doi.org/https://doi.org/10.1029/97JD02083, 1997.

Helbig, N., Mott, R., Van Herwijnen, A., Winstral, A., and Jonas, T.: Parameterizing surface wind speed over complex topography, Journal of Geophysical Research, 122, 651–667, https://doi.org/10.1002/2016JD025593, 2017.

IGN: Geoservices IGN (Open Data), https://geoservices.ign.fr/documentation/index.html, Last accessed on 2021-06-14, 2021.

ISO 2533:1975: Standard Atmosphere, Tech. rep., International Organization for Standardization, 1975.

Iziomon, M. G., Mayer, H., and Matzarakis, A.: Downward atmospheric longwave irradiance under clear and cloudy skies: Measurement and parameterization, Journal of Atmospheric and Solar-Terrestrial Physics, 65, 1107–1116, https://doi.org/10.1016/j.jastp.2003.07.007, 2003.

Jiménez, P. A. and Dudhia, J.: Improving the representation of resolved and unresolved topographic effects on surface wind in the wrf model, Journal of Applied Meteorology and Climatology, 51, 300–316, https://doi.org/10.1175/JAMC-D-11-084.1, 2012.

Jiménez-Muñoz, J. C. and Sobrino, J. A.: A generalized single-channel method for retrieving land surface temperature from remote sensing data, Journal of Geophysical Research: Atmospheres, 108, https://doi.org/10.1029/2003JD003480, 2003.

Jin, M., Li, J., Wang, C., and Shang, R.: A Practical Split-Window Algorithm for Retrieving Land Surface Temperature from Landsat-8 Data and a Case Study of an Urban Area in China, Remote Sensing, 7, 4371–4390, https://doi.org/10.3390/rs70404371, 2015.

Kokhanovsky, A., Lamare, M., Danne, O., Brockmann, C., Dumont, M., Picard, G., Arnaud, L., Favier, V., Jourdain, B., Meur, E. L., Mauro, B. D., Aoki, T., Niwano, M., Rozanov, V., Korkin, S., Kipfstuhl, S., Freitag, J., Hoerhold, M., Zuhr, A., Vladimirova, D., Faber, A.-K., Steen-Larsen, H., Wahl, S., Andersen, J., Vandecrux, B., van As, D., Mankoff, K., Kern, M., Zege, E., and Box, J.: Retrieval of Snow Properties from the Sentinel-3 Ocean and Land Colour Instrument, Remote Sensing, 11, 2280, https://doi.org/10.3390/rs11192280, 2019.

Kokhanovsky, A. A. and Zege, E. P.: Scattering optics of snow, Appl. Optics, 43, 1589–1602, 2004.

Kuipers Munneke, P., van den Broeke, M. R., Reijmer, C. H., Helsen, M. M., Boot, W., Schneebeli, M., and Steffen, K.: The role of radiation penetration in the energy budget of the snowpack at Summit, Greenland, The Cryosphere, 3, 155–165, https://doi.org/10.5194/tc-3-155-2009, http://www.the-cryosphere.net/3/155/2009/, 2009.

Lagouarde, J.-P., Bhattacharya, B. K., Crébassol, P., Gamet, P., Adlakha, D., Murthy, C. S., Singh, S. K., Mishra, M., Nigam, R., Raju, P. V., Babu, S. S., Shukla, M. V., Pandya, M. R., Boulet, G., Briottet, X., Dadou, I., Dedieu, G., Gouhier, M., Hagolle, O., Irvine, M., Jacob, F., Kumar, K. K., Laignel, B., Maisongrande, P., Mallick, K., Olioso, A., Ottlé, C., Roujean, J.-L., Sobrino, J., Ramakrishnan, R., Sekhar, M., and Sarkar, S. S.: Indo-French high-resolution thermal infrared space mission for Earth natural resources assessment and monitoring - Concept and definition of TRISHNA, Int. Arch. Photogramm., XLII-3/W6, 403–407, https://doi.org/10.5194/isprs-archives-XLII-3-W6-403-2019, 2019.

Lamare, M., Dumont, M., Picard, G., Larue, F., Tuzet, F., Delcourt, C., and Arnaud, L.: Simulating optical top-of-atmosphere radiance satellite images over snow-covered rugged terrain, The Cryosphere, 14, 3995–4020, https://doi.org/10.5194/tc-14-3995-2020, 2020.

Larue, F., Picard, G., Arnaud, L., Ollivier, I., Delcourt, C., Lamare, M., Tuzet, F., Revuelto, J., and Dumont, M.: Snow albedo sensitivity to macroscopic surface roughness using a new ray-tracing model, The Cryosphere, 14, 1651–1672, https://doi.org/10.5194/tc-14-1651-2020, 2020.

Lee, W. L., Liou, K. N., and chi Wang, C.: Impact of 3-D topography on surface radiation budget over the Tibetan Plateau, Theoretical and Applied Climatology, 113, 95–103, https://doi.org/10.1007/s00704-012-0767-y, 2013.

Lenot, X., Achard, V., and Poutier, L.: SIERRA: A new approach to atmospheric and topographic corrections for hyperspectral imagery, Remote Sensing of Environment, 113, 1664–1677, https://doi.org/10.1016/j.rse.2009.03.016, 2009.

Leroux, C. and Fily, M.: Modeling the effect of sastrugi on snow reflectance, Journal of Geophysical Research, 103, 25 779, https://doi.org/10.1029/98je00558, 1998.

Lhermitte, S., Abermann, J., and Kinnard, C.: Albedo over rough snow and ice surfaces, The Cryosphere, 8, 1069–1086, https://doi.org/10.5194/tc-8-1069-2014, 2014.

Li, Z.-L., Tang, B.-H., Wu, H., Ren, H., Yan, G., Wan, Z., Trigo, I. F., and Sobrino, J. A.: Satellite-derived land surface temperature: Current status and perspectives, Remote Sensing of Environment, 131, 14–37, https://doi.org/10.1016/j.rse.2012.12.008, 2013.

Libois, Q., Picard, G., Dumont, M., Arnaud, L., Sergent, C., Pougatch, E., Sudul, M., and Vial, D.: Experimental determination of the absorption enhancement parameter of snow, J. of Glaciology, 60, 714–724, https://doi.org/10.3189/2014jog14j015, http://dx.doi.org/10.3189/2014JoG14J015, 2014.

Lliboutry, L.: The Origin of Penitents, J. Glaciol., 2, 331–338, https://doi.org/10.3189/S0022143000025181, 1954.

Marks, D. and Dozier, J.: A clear-sky longwave radiation model for remote alpine areas, Archiv für Meteorologie, Geophysik und Bioklimatologie Serie B, 27, 159–187, https://doi.org/10.1007/BF02243741, 1979.

Martin, E. and Lejeune, Y.: Turbulent fluxes above the snow surface, Annals of Glaciology, 26, 179–183, https://doi.org/10.3189/1998aog26-1-179-183, 1998.

Mattar, C., Durán-Alarcón, C., Jiménez-Muñoz, J. C., Santamaría-Artigas, A., Olivera-Guerra, L., and Sobrino, J. A.: Global Atmospheric Profiles from Reanalysis Information (GAPRI): a new database for earth surface temperature retrieval, International Journal of Remote Sensing, 36, 5045–5060, https://doi.org/10.1080/01431161.2015.1054965, 2015.

Montanaro, M., Gerace, A., Lunsford, A., and Reuter, D.: Stray Light Artifacts in Imagery from the Landsat 8 Thermal Infrared Sensor, Remote Sensing, 6, 10 435–10 456, https://doi.org/10.3390/rs61110435, 2014.

Muñoz Sabater, J.: ERA5-Land hourly data from 1981 to present, https://doi.org/10.24381/cds.e2161bac, 2019.

Neumark, S.: Chapter 3 - Quartic equation, in: Solution of Cubic and Quartic Equations, edited by Neumark, S., pp. 12–24, Pergamon, https://doi.org/https://doi.org/10.1016/B978-0-08-011220-6.50006-8, 1965.

Olson, M., Rupper, S., and Shean, D. E.: Terrain Induced Biases in Clear-Sky Shortwave Radiation Due to Digital Elevation Model Resolution for Glaciers in Complex Terrain, Frontiers in Earth Science, 7, https://doi.org/10.3389/feart.2019.00216, 2019.

Picard, G., Libois, Q., and Arnaud, L.: Refinement of the ice absorption spectrum in the visible using radiance profile measurements in Antarctic snow, The Cryosphere, 10, 2655–2672, https://doi.org/10.5194/tc-10-2655-2016, 2016.

Picard, G., Dumont, M., Lamare, M., Tuzet, F., Larue, F., Pirazzini, R., and Arnaud, L.: Spectral albedo measurements over snow-covered slopes: Theory and slope effect corrections, The Cryosphere, 14, 1497–1517, https://doi.org/10.5194/tc-14-1497-2020, 2020.

Plüss, C. and Ohmura, A.: Longwave radiation on snow-covered mountainous surfaces, Journal of Applied Meteorology, 36, 818–824, https://doi.org/10.1175/1520-0450-36.6.818, 1997.

Pomeroy, J. W., Essery, R. L., and Helgason, W. D.: Aerodynamic and radiative controls on the snow surface temperature, Journal of Hydrometeorology, 17, 2175–2189, https://doi.org/10.1175/JHM-D-15-0226.1, 2016.

Revuelto, J., Lecourt, G., Lafaysse, M., Zin, I., Charrois, L., Vionnet, V., Dumont, M., Rabatel, A., Six, D., Condom, T., Morin, S., Viani, A., and Sirguey, P.: Multi-Criteria Evaluation of Snowpack Simulations in Complex Alpine Terrain Using Satellite and In Situ Observations, Remote Sensing, 10, https://doi.org/10.3390/rs10081171, 2018.

Ricchiazzi, P., Yang, S., Gautier, C., and Sowle, D.: SBDART: A Research and Teaching Software Tool for Plane-Parallel Radiative Transfer in the Earth's Atmosphere, Bulletin of the American Meteorological Society, 79, 2101–2114, https://doi.org/10.1175/1520-0477(1998)079<2101:SARATS>2.0.CO;2, http://journals.ametsoc.org/doi/abs/10.1175/1520-0477%281998%29079%3C2101%3ASARATS%3E2.0.CO%3B2, 1998.

Rotach, M. W. and Zardi, D.: On the boundary-layer structure over highly complex terrain: Key findings from MAP, Quarterly Journal of the Royal Meteorological Society, 133, 937–948, https://doi.org/https://doi.org/10.1002/qj.71, 2007.

Rotach, M. W., Gohm, A., Lang, M. N., Leukauf, D., Stiperski, I., and Wagner, J. S.: On the vertical exchange of heat, mass, and momentum over complex, mountainous terrain, 3, 1–14, https://doi.org/10.3389/feart.2015.00076, 2015.

Sturm, M., Holmgren, J., Koenig, M., and Morris, K.: The thermal conductivity of seasonal snow, J. Glaciol., 43, 26–41, 1997.

Tardy, B., Rivalland, V., Huc, M., Hagolle, O., Marcq, S., and Boulet, G.: A Software Tool for Atmospheric Correction and Surface Temperature Estimation of Landsat Infrared Thermal Data, Remote Sensing, 8, 696, https://doi.org/10.3390/rs8090696, 2016.

Tuzet, F., Dumont, M., Picard, G., Lamare, M., Voisin, D., Nabat, P., Lafaysse, M., Larue, F., Revuelto, J., and Arnaud, L.: Quantification of the radiative impact of light-absorbing particles during two contrasted snow seasons at Col du Lautaret (2058 m a.s.l., French Alps), Cryosphere, 14, 4553–4579, https://doi.org/10.5194/tc-14-4553-2020, 2020.

USGS: How do I rescale Landsat Level-1 digital numbers to reflectance, radiance, and brightness temperature?, https://www.usgs.gov/faqs/how-do-i-rescale-landsat-level-1-digital-numbers-reflectance-radiance-and-brightness?qt-news_science_products=0#, Last accessed on 2021-06-14, 2021.

Varade, D. and Dikshit, O.: Assessment of winter season land surface temperature in the Himalayan regions around the Kullu area in India using landsat-8 data, Geocarto International, 35, 641–662, https://doi.org/10.1080/10106049.2018.1520928, 2020.

Warren, S. G. and Wiscombe, W. J.: A Model for the Spectral Albedo of Snow. II: Snow Containing Atmospheric Aerosols, Journal of the Atmospheric Sciences, 37, 2734–2745, https://doi.org/10.1175/1520-0469(1980)037<2734:amftsa>2.0.co;2, 1980.

Warren, S. G., Brandt, R. E., and O'Rawe Hinton, P.: Effect of surface roughness on bidirectional reflectance of Antarctic snow, Journal of Geophysical Research, 103, 25 789, https://doi.org/10.1029/98je01898, 1998.

Wood, N., Brown, A. R., and Hewer, F. E.: Parametrizing the effects of orography on the boundary layer: An alternative to effective roughness lengths, Quarterly Journal of the Royal Meteorological Society, 127, 759–777, https://doi.org/10.1002/qj.49712757303, 2001.

Yan, G., Wang, T., Jiao, Z., Mu, X., Zhao, J., and Chen, L.: Topographic radiation modeling and spatial scaling of clear-sky land surface
890 longwave radiation over rugged terrain, Remote Sensing of Environment, 172, 15–27, https://doi.org/10.1016/j.rse.2015.10.026, 2016.